Seismically-induced serpentine dehydration as a possible mechanism of water release in subduction zones. Insights from the Alpine Corsica pseudotachylyte-bearing Monte Maggiore ophiolitic unit

Remi Magott, Olivier Fabbri, Marc Fournier

Seismically-induced serpentine dehydration as a possible mechanism of water release in subduction zones. Insights from the Alpine Corsica pseudotachylyte-bearing Monte Maggiore ophiolitic unit

Rémi Magott [1-2]*, Olivier Fabbri [2] and Marc Fournier [3]

1 : CRPG, UMR CNRS 7358, Université de Lorraine, F-54501, Vandœuvre-lès-Nancy, France

2 : Laboratoire Chrono-environnement, UMR CNRS 6249, Univ. Bourgogne Franche-Comté, F-25000 Besançon, France

3 : Sorbonne Universités, UPMC Univ. Paris 06, UMR 7193, ISTEP, F-75005 Paris, France

* Corresponding author: remi.magott@gmail.com
CRPG, UMR CNRS 7358
15, rue Notre-Dame des Pauvres
54500 Vandoeuvre-lès-Nancy
FRANCE

HIGHLIGHTS

- Seismic rupture can propagate through serpentinized peridotite in subducting slabs at 20 to 30 km depths.
- Co-seismic frictional melting can locally dehydrate antigorite into olivine.
- Co-seismic dehydration appears as a possible source of water in subducting slabs.

ABSTRACT

The Monte Maggiore ophiolitic unit of Alpine Corsica consists of an intact to variably hydrated spinel lherzolite intruded by Jurassic gabbro dykes. A widespread serpentinization, marked by low-pressure serpentine polymorphs, results from sea water interaction with mantle rocks during Jurassic sea-floor spreading of the Piemonte-Liguria ocean. A second serpentinization event, marked by the presence of antigorite, is related to the Cretaceous to Paleogene subduction of the Piemonte-Liguria oceanic lithosphere. Tectonic pseudotachylyte veins locally, crosscutting the unit, display several original characteristics. (1) They are hosted by serpentinite, showing that seismic ruptures can propagate through hydrated mantle rocks. (2) The host serpentinite in contact with pseudotachylyte veins shows a thin (500 μm or less) rim of secondary olivine newly crystallized at the expense of serpentine. The heat necessary for serpentine dehydration is likely provided by the frictional melt. Antigorite-bearing clasts (themselves partly dehydrated along their boundaries) reworked in pseudotachylyte veins on one hand and antigorite veins crossing pseudotachylyte veins on the other hand show that frictional melting took place at pressure and temperature conditions compatible with antigorite stability. This indicates that frictional meting occurred at pressures between 0.7 and 0.85 GPa, that is, at ~20 to ~30 km depths in the subducting Piemonte-Liguria oceanic slab. Since the dehydration of serpentine into olivine is only observed at the host-rock selvages of pseudotachylyte veins, it cannot be related to the crossing, by the subducting slab, of the regional 610 ± 100 °C isotherm of the subduction zone, temperature at which antigorite starts to dehydrate into olivine. An estimate of the water released by the dehydration reaction suggests that for a magnitude 6 earthquake, the average amount is about 1.36 L/m^2 or 1.36 x 10^5 m^3 for the entire rupture surface (assumed to be 100 km^2). If the released water is not incorporated in the nearby frictional melt, it can flow away from the slip zone and contribute to the various fluid-rock interactions active in subduction zones. Alternatively, if the water cannot escape from the slip zone and if the pore pressure is locally high enough, it could trigger aftershocks following the initial seismic rupture.

KEYWORDS

Pseudotachylyte, peridotite, serpentinite, subduction, dehydration, olivine, antigorite, Corsica

1. Introduction.

Since the precursor works of Raleigh and Paterson (1965) and Rutter and Brodie (1988), serpentinite dehydration is regarded as a major mechanism to account for intermediate-depth seismicity (70 to 300 km depth, Frohlich, 2006) in subduction zones (Peacock, 2001; Dobson et al., 2002; Hacker et al., 2003; Yamasaki and Seno, 2003; Jung et al., 2004; Nakajima et al., 2009; Ferrand et al., 2017; Wang et al., 2017; Kita and Ferrand, 2018). More specifically, oceanic lithosphere formed along a slow-spreading ridge is expected to experience pervasive and widespread serpentinization. Once such a hydrated lithosphere is subducted at a depth where pressure and temperature conditions are high enough to allow dehydration reactions (Ulmer and Trommsdorff, 1995; Wunder and Schreyer, 1997; Schmidt and Poli, 1998; Guillot et al., 2015), serpentine dehydration can release water which in turn can lead to fault destabilization by decreasing the normal stress acting on fault surfaces (Houston, 2015). This mechanism is referred to as dehydration embrittlement.

In Alpine Corsica, ultramafic and mafic pseudotachylytes are reported from the Cima di Gratera (Austrheim and Andersen, 2004; Andersen and Austrheim, 2006; Andersen et al., 2008; 2014; Deseta et al., 2014; Magott et al., 2016; 2017) and Monte Maggiore ophiolitic units (Magott, 2016; Fabbri et al., 2018). Other reports of ultramafic and mafic pseudotachylytes in the Alpine orogen come from the Moncuni peridotite unit of the Lanzo massif in Italy (Piccardo et al., 2010; Scambelluri et al., 2017). The Cima di Gratera occurrence is interpreted as resulting from intermediate-depth seismicity during the subduction of the Piemonte-Liguria oceanic lithosphere. The Moncuni occurrences were initially interpreted as the result of mid-oceanic ridge faulting during oceanic extension (Piccardo et al., 2010). Based on eclogite facies metamorphic assemblages preserved in the veins, Scambelluri et al. (2017) show that the Lanzo occurrences are likely related to intermediate-depth seismicity in the subducting Piemonte-Liguria lithosphere. In both the Cima di Gratera and Lanzo occurrences, pseudotachylyte veins developed in a fresh (i.e., not serpentinized) peridotite. Conversely, in the Monte Maggiore, the pseudotachylyte veins cross-cut serpentinized peridotite, providing an opportunity to examine interactions between pseudotachylyte and serpentinite.

In this study, we describe evidence for dehydration of serpentinized peridotite by thermal metamorphism caused by tectonic pseudotachylyte. The presence of secondary olivine formed by dehydration of serpentine at the contact with pseudotachylyte veins shows that seismic ruptures can propagate through a hydrated peridotite. The preservation of antigorite, a high-pressure serpentine polymorph, further allows to estimate the depth of

seismicity at the origin of the formation of pseudotachylyte. Lastly, the amount of water released by serpentine dehydration is estimated and the consequences of the water release in the subducting slab are discussed.

2. Geological setting.

In the northwestern end of the Cap Corse peninsula, the Monte Maggiore ultramafic unit consists of a peridotite-dominated ophiolitic thrust sheet belonging to the *Schistes Lustrés* Complex (Fig. 1). It is considered as a remnant of the oceanic lithosphere of the Piemonte-Liguria ocean opened by rifting and slow to ultra-slow spreading during Jurassic to early Cretaceous times (Ohnenstetter et al., 1981; Lagabrielle and Lemoine, 1997; Manatschal and Müntener, 2009; Rampone et al., 2009; Piccardo and Guarnieri, 2010). Mineralogical and geochemical characteristics of the peridotites of the Monte Maggiore unit are similar to those observed in other Alpine ophiolitic units and in present-day oceanic floor peridotite (Piccardo and Guarnieri, 2010; Rampone et al., 2009; Rampone and Hofmann, 2012).

The Monte Maggiore unit is composed of a spinel-plagioclase lherzolite along with clinopyroxene-depleted peridotite and minor dunite (Piccardo and Guarnieri, 2010). The texture is granoblastic. Where preserved, the original mineral assemblage is typical of a spinel lherzolite with olivine > clinopyroxene > orthopyroxene > spinel and minor plagioclase and chromite. Numerous decimeter- to meter-thick gabbroic dykes cross-cut the peridotite. Centimeter-scale chromite pods are also observed. The Monte Maggiore unit is thrust over gneisses of continental origin (Lahondère, 1992; Meresse et al., 2012). The ~~entire~~ Monte Maggiore peridotite is affected by a pervasive tectonic fabric associated with a top-to-the-west sense of shear. This fabric is related to a tectonic deformation during oceanic accretion (Jackson and Ohnenstetter, 1981). It is locally overprinted by an unevenly distributed cataclastic foliation (Fabbri et al., 2018).

The Monte Maggiore peridotite is variably serpentinized. Serpentinization is interpreted as the result of mantle hydration during the opening of the Piemonte-Liguria oceanic basin (Debret, 2013). Primary olivine and, to a lesser extent, pyroxene, are replaced by lizardite, magnetite and minor chrysotile, especially in the southern and the eastern parts of the Monte Maggiore unit (Debret, 2013; Fig. 1). The degree of serpentinization is higher near the tectonic contact with the Centuri gneiss unit (~ 100 %) and decreases northwards (~50 %). Some zones randomly distributed inside the unit are also significantly serpentinized (between 50 and 80 %, Debret, 2013; Fig. 1). Serpentinization appears diffuse throughout the peridotite or localized along veins which do not exceed 20 cm in length and 5 mm in thickness. Thin section observation shows that the diffuse serpentinization corresponds to what is referred to as mesh texture (Viti and Mellini, 1998; Rumori et al., 2004; Andréani et al.,

2007). Serpentine veins are randomly oriented. Based on the cross-cutting relationships between diffuse serpentinization and serpentine veins, Debret (2013) distinguishes three stages of serpentinization. The first stage S1 consists of the isotropic development of lizardite and minor chrysotile associated to magnetite. The second stage S2 consists of the pervasive formation of lizardite and minor chrysotile in mesh texture and the partial substitution of pyroxene (both ortho- and clinopyroxene) by bastite. The development of fibrous lizardite veins is also frequent. Stage S2 serpentinization is the most widespread in the Monte Maggiore unit. The third stage S3 is characterized by the formation of lizardite crack-seal veins and by overgrows of lizardite and chrysotile along the walls of pre-existing lizardite veins. At the scale of the unit, each serpentinization event can be variably developed. All these events are characteristic of an intra-oceanic peridotite serpentinization (Mével, 2003; Andréani et al., 2007; Debret et al., 2013).

In addition to the three stages described by Debret (2013), a fourth stage of serpentinization S4 is observed in the central part of the Monte Maggiore unit, at localities 1 and 2 (Magott, 2016; Fabbri et al., 2018). This stage, characterized by the crystallization of antigorite, can be subdivided into two sub-stages. A sub-stage *S4a* corresponds to a diffuse metamorphic substitution of lizardite by antigorite. A sub-stage *S4b* corresponds to antigorite veins crossing all other structures. The vein-filling antigorite is fibrous~~,~~ and the fibers are perpendicular or highly oblique to the vein walls (Fig. 2). In some instances, several stages of opening can be distinguished (Fig. 2B), suggesting cyclic fluid input and vein opening (crack-seal opening mechanism).

The Monte Maggiore unit was affected by a greenschist facies condition metamorphism. In the peridotite, this metamorphic event is indicated by the partial substitution of pyroxene by tremolite + actinolite + minor chlorite and of olivine by tremolite + chlorite. In the metagabbro dykes, this event is responsible for hornblende overgrowths on primary pyroxene. This first greenschist facies condition event is followed by a blueschist facies condition event attested, in the metagabbro dykes, by the partial replacement of plagioclase by jadeite + zoisite + paragonite + chlorite assemblages (Jackson and Ohnenstetter, 1981; Nicollet et al., 2001). Primary clinopyroxene is commonly rimmed by glaucophane overgrowths. This medium- to high-pressure metamorphic event is interpreted as a consequence of the subduction of the Piemonte-Liguria oceanic lithosphere beneath a continental block or island arc (Nicollet et al., 2001; Molli, 2008; Molli and Malavieille, 2011; Vitale-Brovarone et al., 2013). According to the metagabbro mineralogical assemblages, the peak of metamorphism recorded by the Monte Maggiore unit is about 450°C and 0.85 GPa (Nicollet et al., 2001). A late retrograde greenschist metamorphic facies event tentatively associated with exhumation is evidenced in the metagabbro dykes by rare instances of green hornblende surrounding glaucophane overgrowths (Nicollet et al.,

134 2001; Debret, 2013). The partial substitution of olivine by tremolite and chlorite assemblages is tentatively
135 related to this late retrograde event.

136 In the central part of the Monte Maggiore unit (localities 1, 2 and 3, Fig. 1), the serpentinized peridotite
137 is cross-cut by tectonic pseudotachylyte veins (Magott, 2016). Outcrop-scale, hand-sample scale and thin-
138 section-scale petrographic and structural characteristics of the veins (Fig. 3) are similar to the Cima di Gratera
139 pseudotachylyte occurrence. These similarities suggest that the Monte Maggiore pseudotachylyte occurrence
140 could represent a possible extension of the fossil Wadati-Benioff seismogenic zone described in the Cima di
141 Gratera unit located further south (Fabbri et al., 2018). A characteristic of the Monte Maggiore occurrence is that
142 the formation of pseudotachylyte veins was polyphase, as indicated by numerous cross-cutting relationships
143 between veins and also by the reworking of pseudotachylyte clasts in pseudotachylyte veins. Another
144 characteristic of the Monte Maggiore pseudotachylyte occurrence, which is also observed in the Cima di Gratera
145 occurrence, is that frictional melting occurred concurrently with cataclasis. Some hand sample sections and thin
146 sections show pseudotachylyte fault veins cross-cutting cataclastic serpentinite (Fig. 4), whereas other hand
147 sample sections or thin sections show that cataclasis post-dates frictional melting (Fabbri et al., 2018). In the
148 latter case, cataclasis develops along the boundary between fault veins and the host rock. They form 0.5 to 2.5
149 cm thick, cataclastic layers which, at the hand sample-scale, look like pseudotachylyte fault veins (Fig. 3D).
150 Thin section observation shows that the cataclastic layers contain clasts of pseudotachylyte and that some relict
151 melted rock is preserved along the margin of the layers (Fabbri et al., 2018). These observations indicate that
152 cataclastic layers developed at the expense of pre-existing fault veins. The cataclastic layers and the
153 pseudotachylyte veins are parallel to the cataclastic foliation nearby, if any.

154 **3. Material and methods**

155 Polished thin sections were prepared from oriented samples of ultramafic pseudotachylyte and related host rocks.
156 Thin sections were examined by optical and scanning electron microscopes. Scanning electron microscopy
157 (SEM) was performed at CRPG (Vandœuvre-lès-Nancy, France) and FEMTO-ST (University of Bourgogne-
158 Franche-Comté, Besançon, France). Primary mineral composition was determined with a CAMECA SX100
159 electron microprobe at the SCMEM, University of Lorraine, France. Analyses include bulk matrix (wide beam),
160 wall-rock, non-melted minerals, crystallization products (microlites) as well as serpentinization-related minerals.
161 The determination of serpentine polymorphs was done with RXN1 Raman spectroscopy at the Georessources
162 laboratory (UMR 7359), University of Lorraine, France. Raman analyses were performed on serpentine

polymorphs in the veins and on mesh structures in the host rock. Where serpentine veins are present, the analyses in the host rock were done at different distances to the vein to estimate the importance of serpentinization on both sides of the vein. Serpentine in pseudotachylyte matrix and clasts were also characterized by Raman spectroscopy.

4. Results.

4.1. Microscopic characteristics.

4.1.1. Microscopic characteristics of the serpentinized peridotite hosting the pseudotachylyte veins.

In localities 1 and 2 (Fig. 1), the serpentinized peridotite typically shows an assemblage of serpentine + magnetite + clinopyroxene + orthopyroxene ± rare relict olivine. The olivine site is partly or totally replaced by serpentine. The pyroxene site can be crossed by serpentine veins or can display a weakly developed serpentinization along cleavage planes. Pyroxene pseudomorphozed by serpentine (bastite) is locally observed.

4.1.2. Microscopic characteristics of pseudotachylyte

Where not serpentinized, pseudotachylyte veins are characterized by abundant spherulitic or acicular microlites embedded in a brownish ultrafine-grained or crypto-crystalline matrix (Fig. 4A, B and C, Fig. 5A and F). Polygonal textures suggest that a part of the matrix was glassy, before eventual devitrification. Microlite size ranges between 20 µm and 150 µm. The spatial density and the size of microlites varies from the median part of the vein to the margins (Fig. 5A and E). Vein margins are 80 to 200 mm thick and are characterized by a high density of tiny microlites (< 10µm, Fig. 5A). The central parts of the veins show an increase of the microlite size and an evolution of their crystalline shapes from dendritic or spherulitic shapes toward more mature shapes, especially lath shapes (Fig. 5A and E). The microlites consist of acicular or spherulitic clinopyroxene and subordinate olivine with lath shapes. Fault veins and to a lesser extent injection veins are characterized by variable proportions of clasts (*ca*. 10%). The clasts have sizes between 50 and 800 µm (mean value around 250 µm), are rounded, and consist of assemblages of olivine (commonly partly serpentinized) + serpentine ± pyroxene ± ilmenite (Fig. 4; Fig. 5A and C). Clasts of pseudotachylyte and of polycrystalline aggregates of olivine or pyroxene are also observed (Fig. 4B and Fig. 5D). Some clasts display embayments that are interpreted as corrosion textures (Fig. 5B). In fault veins, clasts close to the wall rock are frequently elongated parallel to the vein boundary. Conversely, the rounded clasts located in the median part of the veins are larger and rarely elongated. Ilmenite clasts are smaller than the clast derived from other minerals, with an average size

191 around 10 µm. The small size of these microlites could be a consequence of a preferential melting of ilmenite
192 which is a mineral characterized by a lower thermal shock resistance than olivine or pyroxene. Extreme
193 comminution due to thermal shock fragmentation could have led to an almost total assimilation of the fragments
194 by the melt, therefore impeding the growth of ilmenite microlites during melt cooling, as proposed by Papa et al.
195 (2018) to account for the scarcity or the small size of garnets microlites in an amphibolite-facies pseudotachylyte
196 occurrence from the western Alps.

197 In the vicinity of secant *S4b* serpentine veins, pseudotachylyte microlites are partly serpentinized (Fig.
198 3C). This serpentinization is characterized by vermicular to fibrous antigorite scattered in the ultrafine-grained or
199 crypto-crystalline matrix or invading microlites and clasts (Fig. 5F). Since this serpentinization is observed next
200 to *S4b* antigorite veins, it is interpreted as relevant to this stage.

201 **4.2. Mineral chemistry and Raman data.**

202 **4.2.1. Mineral chemistry and Raman data of the serpentinized peridotite.**

203 In the fresh (i.e., not serpentinized) peridotite, olivine is characterized by a homogeneous X_{Mg} value
204 between 0.82 and 0.84 (Table 1; Piccardo and Guarnieri, 2010). Clinopyroxene composition is between augite
205 and diopside, but augite composition predominates. Orthopyroxene shows an enstatite composition and includes
206 noticeable amounts of FeO (6 wt.% FeO), Al_2O_3 (4 wt.% Al_2O_3) and minor traces of Cr_2O_3 (between 0.5 and 0.7
207 wt.% Cr_2O_3). The serpentinized peridotite consists of an assemblage of serpentine + magnetite + clinopyroxene
208 + orthopyroxene ± rare olivine. In samples from localities 1 and 2, serpentine is mainly lizardite along with
209 minor amounts of chrysotile, both being partly overprinted by antigorite (Fig. 6A). Stage S4 antigorite is
210 characterized by a X_{Mg} value around 0.89, that is slightly higher than that of primary olivine (Table 1).
211 According to Debret (2013), stage S1 serpentine phases are characterized by an Al_20_3 content between 0.5 and
212 1.0 wt.% and by a FeO content between 3.9 and 6.2 wt.%. The Raman spectra display peaks at 230, 345, 385,
213 465, 620, 687 and 1103 $^{cm-1}$ at low frequency and 3683 and 3705 cm^{-1} at high frequency (Debret, 2013). These
214 peaks are typical of lizardite (Rinaudo and Gastaldi, 2003; Auzende et al., 2004; Groppo et al., 2006). The peak
215 at 3695 cm^{-1} indicates the presence of chrysotile. Stage S2 serpentine phases are characterized by an Al_20_3
216 content between 0.2 and 2.2 wt% and by a FeO content between 2.8 and 7.8 wt%. The Raman spectra are similar
217 to those of lizardite with characteristic peaks at 229, 383, 464, 617, 659 and 1100 cm^{-1} at low frequency and
218 3685 and 3704 cm^{-1} at high frequency. Weak peaks at 3695 cm^{-1} attest of the presence of small amounts of
219 chrysotile (Debret, 2013). Stage S3 serpentine phases, which occur mainly under the form of veins, have an

220 Al_20_3 content between 1.6 to 2.1 wt.% and a Fe0 content between 4.5 to 5.5 wt.%. The Raman spectra are
221 intermediate between lizardite and chrysotile spectra with peaks at 229, 383, 474, 620, 689, 1100 cm^{-1} at low
222 frequency and at 3683, 3690 and 3704 cm^{-1} (Debret, 2013).

223 **4.2.2. Mineral chemistry and Raman data of the pseudotachylyte.**

224 The composition of the pseudotachylyte matrix is close to that of olivine, but includes significant
225 amounts of Al_2O_3 (up to 6.5 wt.%), and minor amounts of CaO (between 2.91 and 3.72 wt.% CaO; Table 2).
226 Cr_20_3, TiO_2 and NiO contents are slightly higher than in host rock primary minerals, with values around 0.15-
227 0.29 wt.% Cr_2O_3, 0.2-0.3 wt.% TiO_2 and 0.08-0.12 wt.% NiO. The matrix also displays X_{Mg} values between 0.78
228 and 0.82. These values are close to those of primary olivine. The absence of plagioclase or orthopyroxene in the
229 microlites or in survivor clasts while they are present in the host rock is due to the lower melting temperature of
230 these minerals This explain these high values by a preferential assimilation of Ca and Al in the melt. The matrix
231 away from *S4b* antigorite veins does not contain any serpentine. On the contrary, the Raman spectra of the
232 pseudotachylyte matrix located close to *S4b* veins (< 0.6 mm) display characteristic peaks of antigorite at 229,
233 379, 461, 378 and 1045 cm^{-1} at low frequency and 3763 and 3700 cm^{-1} at high frequency (Fig. 6D). Additional
234 peaks indicate the presence of olivine (331, 819 and 850 cm^{-1}) and clinopyroxene (1012 cm^{-1}).

235 Microlites of olivine are characterized by X_{Mg} values between 0.80 and 0.85, close to those of primary
236 olivine (0.82). Clinopyroxene microlite composition is between augite and diopside.

237 Raman spectra of serpentine clasts from pseudotachylyte veins are characterized by peaks at 229, 377,
238 458, 683 and 1045 cm^{-1} at low frequency and at 3670 and 3700 cm^{-1} at high frequency (Fig. 6C), indicating a
239 predominance of antigorite (Groppo et al., 2006; Reynard et al., 2015). Peaks at 819 and 850 cm^{-1} indicate the
240 presence of olivine, likely in small amounts (Ishii, 1978; Piriou and MacMillan, 1983). Peaks at 1112 cm^{-1}
241 indicate a small chrysotile component. Serpentine clasts and olivine clasts are characterized by similar X_{Mg}
242 values around 0.82 (Table 2).

243 **4.3. Dehydration of host rock serpentine along pseudotachylyte vein boundaries**

244 **4.3.1. Secondary olivine rims.**

245 In thin sections cut in pseudotachylyte-bearing samples from localities 1 and 2, the host rock sides of
246 pseudotachylyte veins are outlined by thin rims of olivine (Fig. 7A, B, C, E, F and G). Olivine rims are present

where the host rock serpentine is in contact with the vein, but are absent where pseudotachylyte is in contact with pyroxene and spinel. The secondary olivine rims are observed along the boundaries of both fault veins and injection veins (Fig. 7A). Along fault veins, the thickness of secondary olivine rims, laterally variable, is between 70 and 500 µm for fault vein widths between 200 µm and 5 mm. Along injection veins, the thickness of the secondary olivine rims, also laterally variable, is between 70 and 300 µm, for vein widths of about 1 mm or less. The secondary olivine habitus consists of crystals displaying dendritic to acicular shapes or more rarely stubby euhedral shapes (Fig. 7B, C and G). Dendritic olivine is the most common habitus. The dendrites rarely exceed 15 µm in length. In euhedral to subhedral secondary olivine, variations in gray color intensity in the SEM images (Fig. 7G) reflect variations in the Mg number (between 61 and 74, Table. 1). Where the pseudotachylyte vein-host rock boundary is cataclastic, secondary olivine is rare, cataclastic, and the fragments are mixed within serpentine and pyroxene clasts, confirming that cataclasis can post-date pseudotachylyte formation and host-rock serpentine dehydration. Serpentinite survivor clasts in pseudotachylyte veins are surrounded by rims of secondary olivine (Fig. 7D). Secondary olivine is also observed along micro-fractures across clasts (Fig. 7D). Conversely, pyroxene and ilmenite clasts do not display any rim of olivine (Fig. 7B).

The X_{Mg} values of secondary olivine are between 0.61 and 0.74, that is, significantly lower than those of primary olivine which are 0.82 to 0.84 (Table 1). This indicates a significant substitution of Mg by Fe and, therefore, an origin of olivine different from those present in the host rock. The substitution is also observed in the secondary olivine from rims around serpentinite clasts with X_{Mg} values between 0.61 and 0.64, close to those measured in the olivine along pseudotachylyte boundaries (Fig. 7D). These significantly higher FeO contents in olivine around serpentinized clasts or along pseudotachylyte vein boundaries indicate an origin which is different from that of the host rock primary olivine.

Rims of secondary olivine are present where pseudotachylyte is not crossed by late stage serpentine veins (Fig. 2C). Where late serpentine veins (stage S4b) cross-cut pseudotachylyte veins, the pseudotachylyte is affected by serpentinization (Fig. 2C). The nearby host rock is also invaded on a width of about 1 cm.

4.3.2. Post-seismic serpentinization.

The pseudotachylyte veins and secondary olivine rims are cross-cut by late serpentine veins (Fig. 2). These veins have a thickness which does not exceed 250 µm and a lateral extension limited to a few centimeters. The boundaries are sharp. Characteristic Raman peaks at 229, 378, 460, 639, 681 and 1045 cm^{-1} at low frequency and by 3669 and 3701 cm^{-1} at high frequency indicate that the veins are composed of antigorite with a

slight proportion of chrysotile, as attested by a minor peak at 1112 cm^{-1} (Fig. 6B; Rinaudo and Gastaldi, 2003; Auzende et al., 2004; Groppo et al., 2006). On both sides of the antigorite veins, a whitish serpentinization affects the host rock as well as the crossed pseudotachylyte veins over a thickness between 1 and 2.5 mm (Fig. 2). The thickness of the serpentinization halo is proportional to that of the cross-cutting antigorite vein.

In the serpentinization haloes, the unaltered minerals (i.e., preserved during the three first serpentinization stages) are entirely serpentinized (Fig. 3C) by an assemblage of antigorite and chrysotile, as attested in the Raman spectra by peaks at 229, 378, 461, 639, 681, 1047 and 1112 cm^{-1} at low frequency and at 3671 and 3700 cm^{-1} at high frequency (Fig. 6D). Where antigorite veins cross-cut pseudotachylyte veins, the pseudotachylyte matrix and olivine and pyroxene microlites are replaced by a similar assemblage of antigorite ± chrysotile, as indicated by the presence of characteristic peaks in the Raman spectra at 229, 379, 461, 638, 681, 1045 and 1112 cm^{-1} at low frequency and at 3763 and 3700 cm^{-1} at high frequency (Fig.6E). Additional peaks, respectively at 667 and 1012 cm^{-1} at high frequency and at 821 and 843 cm^{-1} at low frequency indicate the presence of relict diopside and olivine in the serpentinization halo.

5. Discussion.

5.1. Relative chronology of serpentinization events and geodynamic significance.

The first three stages of serpentinization S1, S2 and S3 described by Debret (2013) are characterized by the presence of low-temperature and low-pressure serpentine polymorphs. This suggests that these stages occurred during sea floor spreading of the Piemonte-Liguria oceanic lithosphere and concurrent mantle hydration. Stage *S4* succeeding to the first three stages is characterized by the presence of antigorite, which is a high-pressure serpentine polymorph (Ulmer and Trommsdorff, 1995; Wunder and Schreyer, 1997; Evans, 2004; Guillot et al., 2015). It is proposed here that stage *S4* occurred at depth during the subduction of the Piemonte-Liguria lithosphere (Fig. 8).

The presence in not serpentinized pseudotachylyte veins of partly or entirely serpentinized antigorite-bearing clasts surrounded by rims of secondary olivine clearly indicates that the seismic ruptures at the origin of the pseudotachylyte veins took place while stage *S4* antigorite was stable. At the peak pressure and temperature conditions recorded by the Monte Maggiore metagabbro dykes (450°C and 0.85 GPa; Nicollet et al., 2001), antigorite is stable. However, antigorite may have started to form before the serpentinized peridotite reached the peak conditions recorded by the metagabbro assemblages. Indeed, according to Guillot et al. (2015), the

minimum pressure at which antigorite becomes stable is 0.7 GPa, for a temperature of *ca*. 315°C. It follows that *S4* (more precisely *S4a*) serpentinization could have taken place at pressures between 0.7 and 0.85 GPa, that is at depths between *ca*. 20 km and *ca*. 30 km (with a mean serpentinized peridotite density of 3000 $kg.m^{-3}$). Stage *S4b* serpentine veins cross-cutting pseudotachylyte veins (Fig. 8) consist of antigorite, meaning that the Monte Maggiore pseudotachylyte at localities 1 and 2 formed under pressure conditions at which antigorite was still stable. These observations are in agreement for a formation of the Monte Maggiore pseudotachylyte in a subducting slab at depths of 20~30 km.

In pseudotachylyte veins from the Cima di Gratera unit, Austrheim and Andersen (2004) and Andersen and Austrheim (2006) report serpentinite clasts whose rims are partly surrounded by newly crystallized olivine. Although the Mg content of these rims (X_{Mg} ~ 0.90; Austrheim and Andersen, 2004) significantly differs from what is observed at Monte Maggiore (X_{Mg} values between 0.61 and 0.64), it seems that secondary dehydration of hydrated ultramafic clasts is also preserved in the Cima di Gratera unit. A similar conclusion can be reached regarding the pseudotachylyte veins formed under eclogite facies conditions in the Moncuni metaperidotite, Lanzo massif. Indeed, although the depth at which the paleo-earthquakes took place is larger in the Moncuni case than in the Monte Maggiore case (60~70 km *vs*. 20~30 km), Scambelluri et al. (2017) report the presence of antigorite in pseudotachylyte-hosted ultramafic clasts, showing that secondary dehydration of hydrated ultramafic clasts is preserved at Moncuni. Besides, Scambelluri et al. (2017) report the presence, in metaperidotite, of metamorphic olivine formed by the reaction, under eclogite facies conditions.

antigorite + brucite → olivine + fluid.

Since it is not observed only along pseudotachylyte veins, this secondary olivine is clearly metamorphic in origin and is not related to co-seismic slip, at variance with the interpretation presented here.

5.2. ''Co-seismic'' origin of secondary olivine.

Secondary olivine is characterized by X_{Mg} values between 0.61 and 0.74 These values are higher than the X_{Mg} values between 0.82 and 0.84 obtained on primary olivine in the host serpentinized peridotite. This difference in X_{Mg} values can be explained by a preferred assimilation of iron by magnetite commonly associated to antigorite ± chrysotile assemblages in the host rock and indicates that the secondary olivine and the primary magmatic olivine have different origins. Moreover, the presence of rims of iron-rich secondary olivine around most of the serpentine survivor clasts (Fig. 7D) demonstrates that the same process of dehydration as that

observed along the vein boundaries was active around clasts. These observations show a synchronicity between formation of secondary olivine and formation of the pseudotachylyte. It follows that the secondary olivine results from dehydration of serpentine, the heat necessary for dehydration being provided by the co-seismic frictional melt.

5.3. Are secondary olivine rims the result of dehydration embrittlement?

Dehydration embrittlement requires temperature conditions between 500 and 720°C (610 ± 110°C) to dehydrate antigorite into forsterite + talc + H_20 (Ulmer and Trommsdorff, 1995; Peacock, 2001). In the Monte Maggiore unit, the peak temperature and pressure conditions recorded in gabbro dykes are 450°C and 0.85 GPa (Fig. 9; Nicollet et al., 2001). These conditions do not allow dehydration of serpentine (Ulmer and Trommsdorff, 1995; Wunder and Schreyer, 1997). Moreover, no mineral assemblages characterizing regional metamorphic dehydration (enstatite + olivine + Ti-clinohumite + talc; Hoogerduijn-Strating and Vissers, 1991; Scambelluri et al., 1991; Healy et al., 2009) were observed in the Monte Maggiore unit. Therefore, the formation of secondary olivine cannot be associated to a regional metamorphic dehydration such as the one invoked for dehydration embrittlement.

5.4. Other examples of transient thermo-mechanical effects induced by co-seismic frictional melting

The transient thermal effect induced by co-seismic frictional melt on the host hydrated peridotite described here is reminiscent of similar transient thermo-mechanical effects observed in other pseudotachylyte vein occurrences. Three examples are given below. (1) In the immediate vicinity of pseudotachylyte fault veins crossing quartz-feldspar rocks (quartzite and tonalite) in the Alps, Bestmann et al. (2012) describe 50 to 150 μm thick micro-shear zones consisting of ultrafine-grained quartz characterized by a crystal plastic deformation. This ductile deformation was made possible in an otherwise brittle environment by high differential stresses and temperature transients induced by frictional heating for a very short time span (a few seconds) during seismic rupture propagation. Regarding the tonalite case and using TitaniQ thermometry, Bestmann et al. (2016) show that the quartz filling the micro-shear zones was initially deposited by an overheated fluid during the initial stages of co-seismic slip before being plastically deformed. (2) Pittarello et al. (2008) report healed micro-fractures in plagioclase clasts contained in pseudotachylyte related to the Gole Larghe fault zone crossing the Adamello batholith in the Italian Alps. Micro-fracture formation and subsequent healing are inferred to be contemporaneous with co-seismic slip. (3) Heterogeneous melting distribution described by Griffith et al. (2010) along wavy faults in granodioritic and tonalitic host rocks are explained by transient stress perturbations during

co-seismic slip propagation. Frictional melt is preferentially formed along contractional bends because of enhanced normal stresses and tends to accumulate in extensional bends.

5.5. Estimation of the amount of water released by co-seismic serpentine dehydration

At the scale of a subducting slab, especially those slabs formed by slow to ultra-slow oceanic accretion, the in-situ co-seismic dehydration process described here can play a major role in fluid transfers, depending on the size of the rupture surface. Besides, if co-seismic dehydration is considered at the scale of the Wadati-Benioff zone, a significant volume of water can be released by repeated earthquakes. The dehydration reaction serpentine → olivine + talc + H_2O leads to the release of 13 wt.% of water. The amount of water released during propagation of a seismic rupture and slip across a serpentinite mass can be estimated based on the volume of secondary olivine formed during this event. In the following, we attempt to estimate the amount of water released during frictional associated with seismic slip along a fault in serpentinite. The calculation is done in two steps. The first step, which is similar to the analysis followed by Wenk et al. (2000), consists of estimating the thickness of an 'ideal' single pseudotachylyte fault vein that would form along an 'ideal' unique rupture surface. The second step aims at determining the volume of water released by host rock dehydration, based on the thickness of the pseudotachylyte vein that forms in the serpentinized peridotite. Before giving the details of the calculation, the various assumptions and simplifications necessary for the computation are listed below.

5.5.1. Assumptions and simplifications

(1) As mentioned above, the computation is done for an 'ideal' unique fault vein that would form along an 'ideal' unique rupture surface. We therefore neglect the complexity of pseudotachylyte networks reported by many researchers (e.g., Swanson, 1988; Fabbri et al., 2000; Allen, 2005; Di Toro and Pennacchioni, 2005; Rowe et al., 2018).

(2) For the same sake of simplicity as (1), injection veins and associated dehydration are neglected.

(3) The rupture is supposed to nucleate in and propagate across serpentinized peridotite.

(4) The ambient temperature of the serpentinized peridotite hosting the rupture is assumed at 450°C (Nicollet et al., 2001).

(5) The computation is done for a magnitude 6 earthquake. The rupture surface area for such an *M*6 event is typically 100 km^2 (Hanks and Bakun, 2014).

(6) The energy released during the earthquake is mostly converted to heat.

(7) The seismic efficiency η (irradiated energy/total released energy ratio, E_s/E_{tot}) is assumed to be 0.24% (McGarr et al., 1979).

(8) The proportion of survivor clasts is about 10%.

(9) The frictional melt is not super-heated (Di Toro and Pennacchioni, 2004).

(10) The density of the serpentinized peridotite is 3000 $kg.m^{-3}$.

5.5.2. Calculation of the thickness of an 'ideal' single pseudotachylyte vein

Following the calculation of Wenk et al. (2000), we compute the total energy released by the earthquake assuming that most of the energy is converted to heat (assumption (6)). Besides, we compute the energy required to melt one mass unit of peridotite. The total energy released E_{tot} is obtained from E_s, itself obtained from the relationship between surface magnitude M_s and irradiated energy E_s ($\log E_s = 4{,}4 + 1{,}5\ M_s$, E_s in J; Choy and Boatwright, 1995), recalling that the moment magnitude and the surface magnitude are almost identical given the accuracy required here (Das et al., 2011).

We obtain $E_s = 10^{13.4}$ J.

Assuming a seismic efficiency η of 0.24% (assumption (7)), $E_{tot} = E_s/\eta = 1.046 \times 10^{16}$ J.

The energy to melt one mass unit of serpentinized peridotite is:

$$E_{mu} = C_p\ (T_{melt} - T_{initial}) + \Delta H$$

Where C_p is the specific heat at constant pressure (1000 $J.K^{-1}.kg^{-1}$; Kojitani and Akaogi, 1997), T_{melt} is the melting temperature (1700°C; Kojitani and Akaogi, 1997), $T_{initial}$ is the ambient temperature (450°C), and ΔH is the heat of fusion (6×10^5 $J.kg^{-1}$; Kojitani and Akaogi, 1997). Numerical application gives $E_{mu} = 1.85 \times 10^6$ J.

If the proportion of unmelted clasts is about 10% (assumption (8)), the energy required for melting 1 kg of rock becomes $E_{mucorr} = 1.665 \times 10^6$ J.

Dividing E_{tot} by E_{mucorr} gives the mass of pseudotachylyte generated during the *M*6 event, that is,

411 6.28 x 10^9 kg, corresponding to a volume of 2.09 x 10^6 m^3 with a serpentinized peridotite density of 3000 $kg.m^{-3}$
412 (assumption (10)).

413 Assuming that this volume is uniformly distributed over the 100 km^2 of the rupture area through the
414 serpentinized peridotite, the thickness of the 'ideal' fault vein should be 2.09 x 10^{-2} m = 2.09 cm.

415 **5.5.3. Calculation of the quantity of released water.**

416 The water content of serpentine, whatever the polymorph, is about 13 wt %. Optical microscope and
417 SEM observations suggest that the ratio between the fault vein thickness and the width of the dehydrated
418 serpentinite rim on the two sides of the vein is between 0.2 and 0.8, the mean value being 0.5.

419 Isolating 1 m^2 of fault vein inside the serpentinized peridotite, the 2.09 cm thick pseudotachylyte vein
420 would dehydrate a layer of serpentine of 1.045 cm thickness. For one square meter of rupture in the
421 serpentinized peridotite, the maximum amount of released water would be: 1.045 x 10^{-2} m x 13 x 10^{-2} x 1 m^2 =
422 13.585 x 10^{-4} m^3 ~ 1.36 L. If dehydration takes place over the entire rupture surface, the total volume of released
423 water would reach 1.36 x 10^5 m^3.

424 **5.6. Fate of the water released by co-seismic dehydration of serpentine**

425 Regarding the fate of the water released by co-seismic dehydration of serpentine, two end-member
426 scenarios can be considered. (1) As soon as it is released, the water is entirely incorporated (dissolved) in the
427 melt. (2) All the released water escapes from the slip surface. The actual scenario is likely intermediate between
428 these two end-member cases.

429 Observations or arguments in favor of scenario (1) are as follows:

430 - Thermodynamical calculations (Katz et al., 2003) indicate that the weight fraction of H_2O dissolved in a
431 peridotite-derived melt increases with pressure. While it is zero at atmospheric pressure, it reaches ~13
432 wt.% at 1 GPa (Dixon et al., 1995; Mysen and Wheeler, 2000).
433 - According to Andersen and Austrheim (2006), the Cima di Gratera pseudotachylytes are characterized
434 by a high fluid (water) content, as testified by micro-vesicularity in the vein matrix.

435 These considerations indicate that a total or nearly total assimilation of the released water by the co-seismic melt
436 is possible.

If the end-member scenario (2) is valid, then the released water can have various effects, depending on the path it will follow. (i) If the water percolates upwards, it should reach the upper plate and should contribute, with other released fluids, to hydration of the mantle wedge, eventually leading to magma genesis and arc volcanism. (ii) If the water percolates upwards along the subduction interface between the subducting and overlying plates, it can influence the rheology of the rocks present there, enhance chemical transfers and contribute to metasomatic or metamorphic reactions (Angiboust and Agard, 2010; Scambelluri et al., 2015; Bebout and Penniston-Dorland, 2016; Agard et al., 2018). (iii) Local accumulations of fluid along the interface can also trigger slow earthquakes as often observed at depths larger than the down-dip limit of the seismogenic (locked) portions of many subduction zones (Hirose et al., 2010; Obara, 2010; Beroza and Ide, 2011; Franck et al., 2015). (iv) Last but not least, if the released water remains along or near the co-seismic slip surface but without being incorporated in the co-seismic melt, it could, due to its possibly abnormally high pressure at the considered depths, trigger aftershocks. Indeed, since the early work of Nur and Brooker (1972), several observations suggest that over-pressured fluids migrating along or near seismic fault surfaces may be responsible for aftershocks (Li et al., 1987; Bosl and Nur, 2002; Cox and Ruming, 2004; Miller et al., 2004; Micklethwaite, 2008; Waldhauser et al., 2012). The observations described here provide a possible mechanism that could account for fluid-related aftershocks in hydrated mantle rocks. The water released after a large-magnitude event could locally increase the pore pressure and subsequently trigger aftershocks in the vicinity of the main seismogenic fault. The tiny pseudotachylyte veins secant on larger veins observed at localities 1 and 2 could be the result of the largest seismic ruptures among the otherwise small magnitude aftershocks.

6. Conclusion

The Monte Maggiore serpentinized peridotites host pseudotachylyte fault veins, showing that seismic ruptures can propagate through hydrated mantle rocks (serpentinized peridotite or serpentinite). A similar observation has already been reported by Tarling et al. (2018). Such a propagation through a partly hydrated mantle rock can also be inferred from the works of Andersen and Austrheim (2006) and Scambelluri et al. (2017) who describe serpentine-bearing survivor clasts in pseudotachylyte veins from the Cima di Gratera or the Moncuni ultramafic units. However, these observations are not precise enough to demonstrate whether the seismic ruptures nucleated in hydrated mantle rocks or whether they nucleated in non-hydrated rocks (peridotite or gabbro for instance) before propagating through serpentinized peridotite or serpentinite.

Microstructural, petrological and geochemical studies of the Monte Maggiore ultramafic pseudotachylyte veins and their host rock lead to the following results:

1) Along the contact surfaces with pseudotachylyte veins, the host serpentinized peridotite is outlined by rims of secondary olivine resulting from serpentine dehydration induced by frictional heating during seismic faulting.
2) Pseudotachylyte veins include antigorite-bearing clasts and are cross-cut by antigorite veins, indicating that they were formed at pressure and temperature conditions under which antigorite is stable. These conditions consist of a minimum pressure of 0.7 GPa, that is, a minimum depth of ~ 20 km. The maximum depth of formation of antigorite and of pseudotachylyte is constrained by the peak pressure condition recorded by gabbro (0.85 GPa) and is ~30 km.
3) The iron content in secondary olivine is higher than in the primary mantle olivine. The iron enrichment can be accounted for by the reaction magnetite + serpentine (+ brucite + H_2) → olivine + H_20 during the frictional melting-induced dehydration process, magnetite itself being a product of the hydration reaction of pristine mantle olivine.

Assuming an earthquake of magnitude 6 and a simplified model for the Monte Maggiore fossil earthquakes , we estimate, the volume of water released by co-seismic dehydration is estimated at ~ 1.4 L for one square meter of rupture in a serpentinized peridotite for a magnitude 6 event. For the same event, if dehydration takes place over the entire rupture surface (100 km^2), the total volume of released water is estimated at ~ 1.36 x 10^5 m^3. The fate of this water is unknown. It can be entirely assimilated by the melt. Alternatively, it can escape from the seismogenic fault and contribute to mantle wedge hydration or to fluid-rock interactions along the plate interface. It can also play a role in the delayed triggering of slow earthquakes along the plate interface or in the triggering of aftershocks immediately after a large seismic event.

Acknowledgments.

This work was funded by the CNRS-INSU TelluS-ALEAS program. Scanning electron microscopy was supported by the RENATECH network and CRPG (UMR 7358). Constructive comments from two anonymous reviewers helped clarifying the initial version of the manuscript.

493 **References.**

494 Agard, P., Plunder, A., Angiboust, S., Bonnet, G., Ruh, J., 2018. The subduction plate interface: Rock record and
495 mechanical coupling (from long to short time scales). Lithos 320 – 321, 537 – 566. https://doi.org/
496 10.1016/j.lithos.2018.09.029.

497 Allen, J.L., 2005. A multi-kilometer pseudotachylyte system as an exhumed record of earthquake rupture
498 geometry at hypocentral depths (Colorado, USA). Tectonophysics 402, 37 – 54.
499 https://doi.org/10.1016/j.tecto.2004.10.017.

500 Andersen, T.B., Austrheim, H., 2006. Fossil earthquakes recorded by pseudotachylytes in mantle peridotites
501 from the Alpine subduction complex of Corsica. Earth and Planetary Science Letters 242, 58 – 72.

502 Andersen, T.B., Mair, K., Austrheim, H., Podladchikov, Y.Y., Vrijmoed, J.C., 2008. Stress release in exhumed
503 intermediate and deep earthquakes determined from ultramafic pseudotachylyte. Geology 36, 995 – 998.

504 Andersen, T.B., Austrheim, H., Deseta, N., Silkoset, P., Ashwal, L.D., 2014. Large subduction earthquakes
505 along the fossil Moho in Alpine Corsica. Geology 42, 395 – 398. https://doi.org/10.1130/G35345.1

506 Andréani, M., Mével, C., Boullier, A.M., Escartín, J., 2007. Dynamic control on serpentinite crystallization in
507 veins: Constraints on hydration processes in oceanic peridotites. Geochemistry Geophysics Geosystems 8.
508 https://doi.org/10.1029/2006GC001373.

509 Angiboust, S., Agard, P., 2010. Initial water budget: The key to detaching large volumes of eclogitized oceanic
510 crust along the subduction channel? Lithos 120, 453 – 474. https://doi.org/10.1016/j.lithos.2010.09.007.

511 Austrheim, H., Andersen, T.B., 2004. Pseudotachylytes from Corsica: fossil earthquakes from a subduction
512 complex. Terra Nova 16, 193 – 197. https://doi.org/10/1111/j.1365-3121.2004.00551.x.

513 Auzende, A.L., Daniel, I., Reynard, B., Lemaire, C., Guyot, F., 2004. High-pressure behavior of serpentine
514 minerals: a Raman spectroscopic study. Physics and Chemistry of Minerals 31, 269 – 277.

515 Bebout, G.E., Penniston-Dorland, S.C., 2016. Fluid and mass transfer at subduction interfaces – The field
516 metamorphic record. Lithos 240 – 243, 228 – 258. https://doi.org/10.1016/j.lithos.2015.10.007.

517 Beroza, G.C., Ide, S., 2011. Slow earthquakes and nonvolcanic tremor. Annual Review of Earth and Planetary
518 Sciences 39, 271 – 296. https://doi.org/10.1146/annurev-earth-040809-15253.

519 Bestmann, M., Pennacchioni, G., Nielsen, S., Göken, M., De Wall, H., 2012. Deformation and ultrafine dynamic
520 recrystallization of quartz in pseudotachylyte-bearing brittle faults: A matter of a few seconds. Journal of
521 Structural Geology 38, 21 – 38. https://doi.org/10.1016/j.jsg.2011.10.001.

522 Bestmann, M., Pennacchioni, G., Mostefaoui, S., Göken, M., de Wall, H., 2016. Instantaneous healing of micro-
523 fractures during coseismic slip: Evidence from microstructure and Ti in quartz geochemistry within an exhumed
524 pseudotachylyte-bearing fault in tonalite. Lithos 254, 84 – 93. https://doi.org/10.1016/j.lithos.03.011.

525 Bosl, W.J., Nur, A., 2002. Aftershocks and pore fluid diffusion following the 1992 Landers earthquake. Journal
526 of Geophysical Research 107, 2366. https://doi.org/10.1029/2001JB000155.

527 Choy, G.L., Boatwright, J.L., 1995. Global patterns of radiated seismic energy and apparent stress. Journal of
528 Geophysical Research 100, 18205 – 18228.

529 Cox, S.F., Ruming, K., 2004. The St Ives mesothermal gold system, Western Australia-a case of golden
530 aftershocks? Journal of Structural Geology 26, 1109 – 1125.

531 Das, R., Wason, H.R., Sharma, M. L., 2011. Global regression relations for conversion of surface wave and body
532 wave magnitudes to moment magnitude. Natural Hazards 59, 801 – 810.

533 Debret, B., 2013. Serpentinites, vecteurs des circulations fluides et des transferts chimiques de l'océanisation à la
534 subduction : exemple dans les Alpes occidentales. Clermont-Ferrand University PhD Thesis, 454 pp.

535 Debret, B., Nicollet, C., Andreani, M., Schwartz, S., Godard, M., 2013. Three steps of serpentinization in an
536 eclogitized oceanic serpentinization front (Lanzo Massif – Western Alps). Journal of Metamorphic Geology 31,
537 165 – 186. https://doi.org/10.1111/jmg.12008.

538 Deseta, N., Andersen, T.B., Ashwal, L.D., 2014. A weakening mechanism for intermediate-depth seismicity?
539 Detailed petrographic and microstructural observation from blueschist facies pseudotachylytes, Cape Corse,
540 Corsica. Tectonophysics 610, 138 – 149.

541 Di Toro, G., Pennacchioni, G., 2004. Superheated friction-induced melts in zoned pseudotachylytes within the
542 Adamello tonalites (Italian Southern Alps). Journal of Structural Geology 26, 1783 – 1801.

543 Di Toro, G., Pennacchioni, G., 2005. Fault plane processes and mesoscopic structure of a strong-type
544 seismogenic fault in tonalites (Adamello batholith, Southern Alps). Tectonophysics 402, 55 – 80.

545 Dixon, J., Stolper, E., Holloway, J., 1995. An experimental study of water and carbon dioxide solubilities in mid
546 ocean ridge basaltic liquids: I. Calibration and solubility models. J. Petrol. 36, 1607 – 1631.

547 Dobson, D.P., Meredith, P.G., Boon, S.A., 2002. Simulation of subduction zone seismicity by dehydration
548 embrittlement. Science 298, 1407 – 1410.

549 Evans, B.W., 2004. The serpentinite multisystem revisited: chrysotile is metastable. International Geology
550 Review 46, 479 – 506.

551 Fabbri, O., Lin, A., Tokushigé, H., 2000. Coeval formation of cataclasite and pseudotachylyte in a Miocene
552 forearc granodiorite, southern Kyushu, Japan. Journal of Structural Geology, 22 1015 – 1025.

553 Fabbri, O., Magott, R., Fournier, M., Etienne, L., 2018. Pseudotachylyte in the Monte Maggiore ophiolitic unit
554 (Alpine Corsica): A lateral extension of the Cima di Gratera intermediate-depth Wadati-Benioff paleo-seismic
555 zone. Bulletin de la Société Géologique de France 189, 1 – 17. https://doi.org/10.1051/bsgf/2018020.

556 Ferrand, T., Hilairet, N., Incel, S., Deldicque, D., Labrousse, L., Gasc, J., Renner, R., Wang, Y., Green, H.W.,
557 2017. Dehydration-driven stress transfer triggers intermediate-depth earthquakes. Nature Communications 8,
558 15247 – 15258.

559 Frank, W.B., Shapiro, N.M., Husker, A.L., Kostoglodov, V., Bhat, H.S., Campillo, M., 2015. Along-fault pore-
560 pressure evolution during a slow-slip event in Guerrero, Mexico. Earth and Planetary Science Letters 413, 135 –
561 143. https://doi.org/10.1016/j.epsl.2014.12.051.

562 Griffith, W.A., Nielsen, S., Di Toro, G., Smith, S.A., 2010. Rough faults, distributed weakening, and off-fault
563 deformation. Journal of Geophysical Research 115, B08409. https://doi.org/10.1029/2009JB006925.

564 Groppo, C., Rinaudo, C., Cairo, S., Gastaldi, D., Compagnoni, R., 2006. Micro-Raman spectroscopy for a quick
565 and reliable identification of serpentine minerals from ultramafics. European Journal of Mineralogy 18, 319 –
566 329.

567 Guillot, S., Schwartz, S., Reynard, B., Agard, P., Prigent, C., 2015. Tectonic significance of serpentinites.
568 Tectonophysics 646, 1 – 19.

569 Hacker, B. R., Peacock, S.M., Abers, G.A., Holloway, S.D., 2003. Subduction Factory 2. Are intermediate-depth
570 earthquakes in subducting slabs linked to metamorphic dehydration reactions? Journal of Geophysical Research
571 108. https://doi.org/10.1029/2001JB001129.

572 Hanks, T.C., Bakun, W.H., 2014. M–log A models and other curiosities. Bulletin of the Seismological Society of
573 America 104, 2604 – 2610.

574 Healy, D., Reddy, S.M., Timms, N.E., Gray, E.M., 2009. Trench-parallel fast axes of seismic anisotropy due to
575 fluid-filled cracks in subducting slabs. Earth and Planetary Science Letters 283, 75 – 86.

576 Hirose, H., Asano, Y., Obara, K., Kimura, T., Matsuzawa, T., Tanaka, S., Maeda, T., 2010. Slow earthquakes
577 linked along dip in the Nankai subduction zone. Science 330, 1502 – 1502.

578 Hoogerduijn-Strating, E.H., Vissers, R.L.M., 1991. Dehydration-induced fracturing of eclogite-facies
579 peridotites: implication for the mechanical behavior of subduction oceanic lithosphere. Tectonophysics 200, 187
580 – 198.

581 Houston, H., 2015. Deep Earthquakes. In: G. Schubert (editor) Treatise on Geophysics, 2nd edition, Vol. 4.
582 Elsevier, Oxford, 329-354.

583 Ishii, K., 1978. Lattice dynamics of forsterite. American Mineralogist 63, 1198 – 1208.

584 Jackson, M.D., Ohnenstetter, M., 1981. Peridotite and gabbroic structures in the Monte Maggiore massif, Alpine
585 Corsica. The Journal of Geology 89, 703 – 719.

586 Jung, H., Green, H.W., Dobrzhinetskaya, L.F., 2004. Intermediate-depth earthquake faulting by dehydration
587 embrittlement with negative volume change. Nature 428, 545 – 549.

588 Katz, R.F., Spiegelman, M. Langmuir, C.H., 2003. A new parameterization of hydrous mantle melting.
589 Geochemistry, Geophysics, Geosystems, 4, 1073. https://doi.org/10.1029/2002GC000433.

590 Kita, S., Ferrand, F., 2018. Physical mechanisms of mantle earthquakes: Comparison of natural and experimental
591 events. Scientific Reports 8, 17049. https://doi.org/10.1038/s41598-018-35290-x.

592 Kojitani, H., Akaogi, M., 1997. Melting enthalpies of mantle peridotite: calorimetric determinations in the
593 system CaO-MgO-Al_2O_3-SiO_2 and application to magma generation. Earth and Planetary Science Letters 153,
594 209 – 222.

595 Lagabrielle, Y., Lemoine, M., 1997. Alpine, Corsican and Apennine ophiolites: the slow-spreading ridge model.
596 Comptes Rendus de l'Académie des Sciences 325, 909 – 920.

597 Lahondère J.C., 1992. Carte géologique de la France au 1/50000. Feuille de Luri. BRGM.

598 Li, V.C., Seale, S.H., Cao, T., 1987. Post-seismic stress and pore pressure readjustment and aftershock
599 distributions. Tectonophysics 144, 37-54.

600 Magott, R., 2016. Propagation de la rupture sismique dans la lithosphère océanique: une étude basée sur
601 l'analyse structurale des cataclasites et pseudotachylytes jalonnant les failles dans les roches mafiques et
602 ultramafiques accrétées ou obductées sur les continents. L'exemple corse. Franche-Comté University PhD
603 Thesis, 255 pp.

604 Magott, R., Fabbri, O., Fournier, M., 2016. Subduction zone intermediate-depth seismicity: Insights from the
605 structural analysis of Alpine high-pressure ophiolite-hosted pseudotachylytes (Corsica, France). Journal of
606 Structural Geology 87, 95 – 114. https://doi.org/10.1016/j.jsg.2016.04.002.

607 Magott, R., Fabbri, O., Fournier, M., 2017. Polyphase ductile/brittle deformation along a major tectonic
608 boundary in an ophiolitic nappe, Alpine Corsica: Insights on subduction zone intermediate-depth asperities.
609 Journal of Structural Geology 94, 240 – 257. https://doi.org/10.1016/j.jsg.2016.12.002.

610 Meresse, F., Lagabrielle, Y., Malavieille, J., Ildefonse, B., 2012. A fossil Ocean-Continent Transition of the
611 Mesozoic Tethys preserved in the Schistes Lustrés nappe of northern Corsica. Tectonophysics 579, 4 – 16.

612 Manatschal, G., Müntener, O., 2009. A type sequence across an ancient magma-poor ocean-continent transition:
613 the example of the western Alpine Tethys ophiolites. Tectonophysics 473, 4 – 19.

614 McGarr, A., Spottiswoode, S.M., Gay, N.C., Ortlepp, W.D., 1979. Observations relevant to seismic driving
615 stress, stress drop, and efficiency. Journal of Geophysical Research 84, 2251 – 2261.

616 Mével, C., 2003. Serpentinization of abyssal peridotites at mid-ocean ridges. Comptes Rendus Geosciences 335,
617 825 – 852.

618 Micklethwaite, S., 2008. Optimally oriented ''fault-valve'' thrusts: Evidence for aftershock-related fluid
619 pressure pulses? Geochemistry, Geophysics, Geosystems, 9, Q04012. https://doi.org/10.1029/2007GC001916.

620 Miller, S.A., Collettini, C., Chiaraluce, L., Cocco, M., Barchi, M., Kaus, B.J., 2004. Aftershocks driven by a
621 high-pressure CO_2 source at depth. Nature, 427, 724 – 727.

622 Molli, G., Malavieille, J., 2011. Orogenic processes and the Corsica / Apennine geodynamic evolution: Insight
623 from Taiwan. International Journal of Earth Science 100, 1207 – 1224. https://doi.org/10.1007/s00531-010-
624 0598-y.

625 Molli, G., 2008. Northern Apennine-Corsica orogenic system: an updated overview. Geological Society,
626 London, Special Publications 298, 413 – 442.

627 Mysen, B., Wheeler, K., 2000. Solubility behavior of water in haploandesitic melts at high pressure and high
628 temperature. Am. Mineral., 85, 1128 – 1142.

629 Nakajima, J., Tsuji, Y., Hasegawa, A., Kita, S., Okada, T., Matsuzawa, T., 2009. Tomographic imaging of
630 hydrated crust and mantle in the subducting Pacific slab beneath Hokkaido, Japan: Evidence for dehydration
631 embrittlement as a cause of intraslab earthquakes. Gondwana Research 6, 470 – 481.

632 Nicollet, C., Chazot, G., Cloquet, C., 2001. Evolution géodynamique d'une portion du manteau : Pétrologie et
633 trajet P-T des lherzolithes et gabbro associés du Monte Maggiore, Cap Corse. Journée de la Société Géologique
634 de France, Clermont-Ferrand.

635 Nur, A., Booker, J.R., 1972. Aftershocks caused by pore fluid flow? Science 175, 885 – 887.

636 Obara, K., 2010. Phenomenology of deep slow earthquake family in southwest Japan: Spatio-temporal
637 characteristics and segmentation. Journal of Geophysical Research 115, B00A25.
638 https://doi.org/10.1029/2008JB006048.

639 Ohnenstetter, M., Ohnenstetter, D., Vidal, P., Cornichet, J., Hermitte, D., Mace, J. 1981. Crystallization and age
640 of zircon from Corsican ophiolitic albitites: consequences for oceanic expansion in Jurassic times. Earth and
641 Planetary Science Letters 54, 397 – 408.

642 Papa, S., Pennacchioni, G., Angel, R.J., Faccenda, M., 2018. The fate of garnet during (deep-seated) coseismic
643 frictional heating: The role of thermal shock. Geology 46, 471 – 474. https://doi.org/10.1130/G40077.1.

644 Peacock, S.M., 2001. Are the lower plane of double seismic zones caused by serpentine dehydration in
645 subducting oceanic mantle? Geology 29, 299 – 302.

646 Piccardo, G.B., Ranalli, G., Guarnieri, L., 2010. Seismogenic shear zone in the lithospheric mantle: Ultramafic
647 pseudotachylyte in the Lanzo Peridotite (Western Alps, NW Italy). Journal of Petrology 51, 81 – 100.

648 Piccardo, G.B., Guarnieri, L., 2010. The Monte Maggiore peridotite (Corsica, France): a case study of mantle
649 evolution in the Ligurian Tethys. Geological Society London Special Publications 337, 7 – 45.

650 Piriou, B., MacMillan, P., 1983. The high-frequency vibrational spectra of vitreous and crystalline orthosilicates.
651 American Mineralogist 68, 426 – 443.

652 Pittarello, L., Di Toro, G., Bizzarri, A., Pennacchioni, G., Hadizadeh, J., Cocco, M., 2008. Energy partitioning
653 during seismic slip in pseudotachylyte-bearing faults (Gole Larghe Fault, Adamello, Italy). Earth and Planetary
654 Science Letters 269, 131 – 139.

655 Raleigh, C.B., Paterson, M.S., 1965. Experimental deformation of serpentinite and its tectonic implications.
656 Journal of Geophysical Research 70, 3965 – 3985.

657 Rampone, E., Hofmann, A.W., Raczek, I., 2009. Isotopic equilibrium between mantle peridotite and melt:
658 Evidence from the Corsica ophiolite. Earth and Planetary Science Letters 288, 601 – 610.

659 Rampone, E., Hofmann, A.W., 2012. A global overview of isotopic heterogeneities in the oceanic mantle. Lithos
660 148, 247 – 261.

661 Reynard, B., Bezacier, L., Caracas, R., 2015. Serpentines, talc, chlorites and their high-pressure phase
662 transitions: a Raman spectroscopic study. Physics and Chemistry of Minerals 42, 641 – 649.

663 Rinaudo, C., Gastaldi, D., 2003. Characterization of chrysotile, antigorite and lizardite by FT-Raman
664 spectroscopy. The Canadian Mineralogist 41, 883 – 890.

665 Rowe, C.D., Ross, C., Swanson, M.T., Pollock, S., Backeberg, N., Barshi, N.A., Bate, C.E., Carruthers, S.,
666 Coulson, S., Dascher-Cousineau, K., Harrichhausen, N., Peña Castro, A.F., Nisbet, H., Rakoczy, P., Scibek, J.,
667 Smith, H., Tarling, M.S., Timofeev, A., Young, E., 2018. Geometric complexity of earthquake rupture surfaces
668 preserved in pseudotachylyte networks. Journal of Geophysical Research 123, 7998 – 8015.
669 https://doi.org/10.1029/2018JB016192.

670 Rumori, C., Mellini, M., Viti, C., 2004. Oriented, non-topotactic olivine → serpentine replacement in mesh-
671 textured, serpentinized peridotites. European Journal of Mineralogy, 16, 731 – 741.

672 Rutter, E.H., Brodie, K.H., 1988. Experimental ‘’syntectonic’’ dehydration of serpentinite under condition of
673 controlled pore water pressure. Journal of Geophysical Research 93, 4907 – 4932.

674 Scambelluri, M., Hoogerduijn-Strating, E.H., Piccardo, G., Vissers, R.L.M., Rampone, E., 1991. Alpine olivine
675 and clinohumite-bearing assemblages in the Erro-Tobbio peridotite (Voltri Massif, NW Italy). Journal of
676 Metamorphic Geology 9, 79 – 105.

677 Scambelluri, M., Pettke, T., Cannao, E., 2015. Fluid-related inclusions in Alpine high-pressure peridotite reveal
678 trace element recycling during subduction-zone dehydration of serpentinized mantle. Earth and Planetary
679 Science Letters 429, 45 – 59. https://doi.org/10.1016/j.epsl.2015.07.060.

Scambelluri, M., Pennacchioni, G., Gilio, M., Bestmann, M., Plümber, O., Nestola, F., 2017. Fossil intermediate-depth earthquakes in subducting slabs linked to differential stress release. Nature geoscience 10, 960 – 966.

Schmidt, M.W., Poli, S., 1998. Experimentally based water budgets for dehydrating slabs and consequences for arc magma generation. Earth and Planetary Science Letters 163, 361 – 379. https://doi.org/10.1016/S0012-821X(98)00142-3.

Swanson, M.T., 1988. Pseudotachylyte-bearing strike-slip duplex structures in the Fort Foster Brittle Zone, S. Maine. Journal of Structural Geology 10, 813 – 828.

Tarling, M.S., Smith, S.A.F., Viti, C., Scott, J.M., 2018. Dynamic earthquake rupture preserved in a creeping serpentinite shear zone. Nature communications 9, 3552. https://doi.org/10.1038/s41467-018-05965-0.

Ulmer, V., Trommsdorff, P., 1995. Serpentine stability to mantle depth and subduction-related magmatism. Science 268, 858 – 861.

Vitale-Brovarone, A., Beyssac, O., Malavieille, J., Molli, G., Beltrando, M., Compagnoni, R., 2013. Stacking and metamorphism of continuous segments of subducted lithosphere in a high-pressure wedge: The example of Alpine Corsica (France). Earth-Science Reviews 116, 35 – 56.

Viti, C., Mellini, M., 1998. Mesh textures and bastites in the Elba retrograde serpentinites. European Journal of Mineralogy 10, 1341 – 1359.

Waldhauser, F., Schaff, D.P., Diehl, T., Engdahl, R.E., 2012. Splay faults imaged by fluid-driven aftershocks of the 2004 M_w 9.2 Sumatra-Andaman earthquake. Geology 40, 243 – 246. https://doi.org/10.1130/G32420.1.

Wang, J., Zhao, D., Yao, Z., 2017. Seismic anisotropy evidence for dehydration embrittlement triggering intermediate-depth earthquakes. Scientific Reports 7, 2613 – 2622.

Wenk, H.R., Johnson, L.R., Ratschbacher, L., 2000. Pseudotachylites in the Eastern Peninsular Ranges of California. Tectonophysics 321, 253 – 277.

Wunder, B., Schreyer, W. (1997). Antigorite: High-pressure stability in the system MgO-SiO_2-H_2O (MSH). Lithos, 41, 213 – 227. https://doi.org/10.1016/S0024-4937(97)82013-0.

Yamasaki, T., Seno, T., 2003. Double seismic zone and dehydration embrittlement of the subducting slab. Journal of Geophysical Research 108. https://doi.org/10.1029/2002JB001918.

Table captions

Table 1. Chemical composition of secondary olivine in dehydrated rims and host rock (serpentinized and non-serpentinized). NS: non-serpentinized, SP: serpentinized.

Table 2. Average composition of pseudotachylyte components.

Figure captions

Fig. 1. A: Simplified geological map of the study area (modified after Debret, 2013). B: A-A' cross-section.

Fig. 2. Relationships between *S4* serpentine veins, serpentinite host rock and pseudotachylyte veins. A. Late *S4b* fibrous antigorite (*Late Ant vein*) crossing pseudotachylyte (*Pst*) vein and serpentinite wallrock (*Serp wallrock*), locality 2. B. Zoned *S4b* antigorite vein (*Late Ant vein*) crossing partly serpentinized pseudotachylyte (*Serp Pst*) and serpentinized wallrock (*Serp wallrock*), locality 1. C. Late *S4b* antigorite vein (*Late Ant vein*) cross-cutting serpentinized peridotite and a pseudotachylyte vein. On each side of the antigorite vein, a serpentinization halo invades the wallrock. Invasion is deeper in the host serpentinite (about 750 μm) than in the pseudotachylyte (200 μm).

Fig. 3. Photographs of serpentinized peridotite outcrops and hand samples crossed by pseudotachylyte veins. A. Anastomosed fault vein network (*Pst networks*), locality 1. The veins show a positive relief. B. Isolated fault veins, locality 1. C. Serpentinite hand sample showing a fault vein (*Fv*) flanked by injection veins (*Iv*), locality 2. D. Serpentinitized peridotite (*Serp peridotite*) hand sample showing pseudotachylyte fault veins (*Pst*) and a pseudotachylyte vein-looking cataclastic zone (*Ct*), locality 2.

Fig. 4: Photomicrographs of pseudotachylyte and host serpentinite, locality 2. A. Flow folds in an injection vein reworking pyroxene and serpentinized olivine clasts (*Serp Ol clast*). B. Clast of reworked pseudotachylyte (*Pst clast*) with embayment (*Emb*). C. Pseudotachylyte matrix showing a polygonal texture due to devitrification. D. Pseudotachylyte fault vein (*Fv*) and associated injection vein (*Iv*). The serpentinite host rock below the fault vein is cataclastic (*Ct*). E. Pseudotachylyte fault vein (*Fv*) crossing a cataclastic serpentinite (*Ct*). F. Cataclastic serpentinite cross-cut by an early pseudotachylyte vein (*Early pst*) itself cross-cut by a late pseudotachylyte vein (*Late pst*).

733 Fig. 5. SEM images of pseudotachylyte veins in partly serpentinized peridotite, locality 1. A. Pseudotachylyte
734 fault vein (*Pst*) with serpentinized wall rock. From the lower left corner of the image to its upper right corner, the
735 size of microlites increases from the chilled margin (*Cm*, lower left) where microlites are small to the median
736 part of the vein where microlites are larger (upper right). The square is the area enlarged in C. B. Rounded clasts
737 of olivine displaying embayments. C. Clast of olivine (*Ol clast*) surrounded by olivine overgrowths with a comb
738 structure. D. Clast of pseudotachylyte (*Pst clast*) reworked in a younger pseudotachylyte (*Pst*). Note the large
739 embayment almost crossing the entire clast. E. Olivine and clinopyroxene microlites with acicular shapes near
740 the chilled margin (*Cm*) or with lath shapes (near the median part of the vein). F. Enlargement of
741 pseudotachylyte matrix showing rounded olivine clasts, acicular clinopyroxene microlites and serpentinized
742 matrix (*Sz Matrix*).

743 Fig. 6. Raman spectra of serpentine phases obtained on pseudotachylyte fault veins, host rocks and late secant
744 serpentine veins, locality 2. For each spectrum, the signal is analyzed on two acquisition spectral windows and
745 the characteristic bands are indicated. A. Raman spectrum of the serpentinite hosting a pseudotachylyte vein and
746 showing diffuse antigorite tentatively related to stage S4a (sample depicted in Fig. 3C). B. Raman spectrum of
747 late antigorite veins related to stage S4b (sample depicted in Fig. 3C). The spectrum indicates a dominant
748 antigorite composition and a minor chrysotile component. C. Raman spectrum of the central part of a
749 serpentinite survivor clast reworked in a pseudotachylyte vein and surrounded by secondary olivine. The
750 spectrum indicates the presence of stage S4a antigorite (diffuse in the clast and not under the form of vein
751 filling). D. Raman spectrum indicating the presence of *S4b* antigorite in the serpentinized halo of the wall-rock
752 at a distance of ~ 250 µm away from a late antigorite vein. E. Raman spectrum indicating the presence of *S4b*
753 antigorite in the matrix of a pseudotachylyte vein crossed by a late antigorite vein. Raman analysis is done at a
754 distance of ~ 250 µm from the antigorite vein.

755 Fig. 7. SEM images of secondary olivine rims along the boundaries between pseudotachylyte and host
756 serpentinite or reworked clasts. A. Secondary olivine rim developed along the boundaries between host
757 serpentinite (*Wall*) and injection and fault veins (*Pst*). To the left, the pseudotachylyte is in contact with
758 ultracataclasite (*Uct*) itself in contact with cataclasite (*Ct*). Both cataclasite and ultracataclasite consist of
759 fragments of serpentine mixed with fragments of secondary olivine. B. Secondary olivine rim (*Sec Ol*, right
760 side of the image) showing clusters of dendritic secondary olivine (*DSO*) and acicular secondary olivine
761 (*ASO*). Where it is not acicular or dendritic, the olivine is more massive, but the precise shape of the

762 crystals (euhedral or anhedral) cannot be determined. In the upper part of the image, a horizontal antigorite
763 vein crossing (1) the serpentinite host rock (*Wall*), (2) the secondary olivine rim (*Sec Ol*) and (3) the
764 pseudotachylyte vein (*Pst*) is attributed to the serpentinization stage S4b. *Il clast*: clast of ilmenite. C:
765 Enlargement of the secondary olivine rim of (B) highlighting ~~the~~ dendritic secondary olivine (*DSO*) acicular
766 secondary olivine (*ASO*). D. Antigorite rounded clast (*Ant Clast*) surrounded by a rim of secondary olivine (*Sec*
767 *Ol*) in a pseudotachylyte vein (*Pst*). E. Secondary olivine rim (*Sec Ol*) along the boundary between serpentinite
768 host rock (*Wall*) and a pseudotachylyte fault vein (*Pst*). The rectangle is the area enlarged in F. F. Secondary
769 olivine rim (*Sec Ol*) displaying rectangular olivine crystals with long axes parallel to the host rock-
770 pseudotachylyte vein (*Pst*) boundary. G. Secondary olivine rim (*Sec Ol*) between wall rock (*Wall*) and a
771 pseudotachylyte vein (*Pst*). Inside the rim, differences in grey intensity reflects differences in the X_{Mg} of olivine
772 crystals (between 0.61 and 0.69). Subhedral secondary olivines are best developed in the largest part of the
773 dehydrated border.

774 Fig. 8. Relative chronology of serpentinization events and seismogenic ruptures. A. Fresh (i.e., not
775 serpentinized) spinel peridotite equilibrated in the plagioclase domain before seafloor spreading (Piccardo and
776 Guarnieri, 2010). B. First stages of serpentinization (stages S1 to S3) related to sea water-mantle rock
777 interactions and characterized by low-pressure lizardite and chrysotile assemblages. C. High pressure
778 serpentinization stage (stage S4a) characterized by the development of antigorite ± chrysotile assemblages at the
779 expense of stages S1 to S3 lizardite and chrysotile assemblages. D. Seismic ruptures causing the formation of
780 frictional melt and associated dehydration. E. Formation of antigorite veins (S4b) post-dating S1 to S4a
781 serpentinization events and pseudotachylyte vein formation.

782 Fig. 9. P-T pathway of the Monte Maggiore peridotite unit projected on various mineralogical reactions
783 (modified after Nicollet et al., 2001). Mantle upwelling refers to the adiabatic upwelling and decompression of
784 the asthenosphere.

785 Fig. 10. Simplified geodynamical setting of co-seismic dehydration of serpentinite in the subducting Piemonte-
786 Liguria oceanic lithosphere (Monte Maggiore unit) and associated water release. A. General sketch showing the
787 eastward-dipping subduction of the Piemonte-Liguria oceanic plate under a micro-block or an island arc
788 (Cretaceous to Paleogene times). B. Three scenarios of seismic rupture nucleation and propagation: (1) in non-
789 hydrated peridotite, (2) in mixed non-hydrated and hydrated peridotite, (3) in hydrated peridotite. C. Co-seismic
790 dehydration of hydrated peridotite at Monte Maggiore following scenario (3) and subsequent water release.

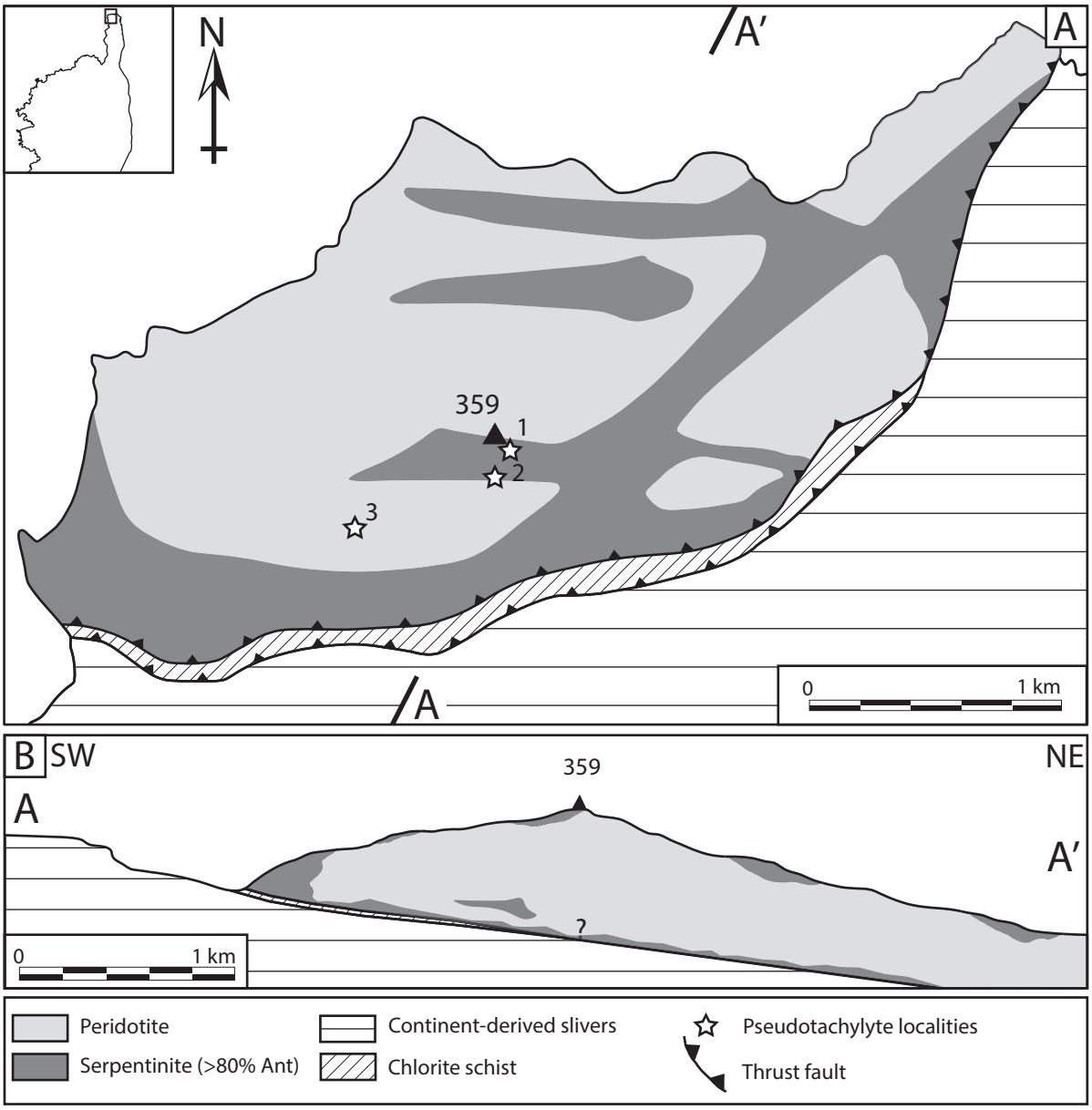
N
A'
A
359
1
2
3
0
1 km
A
B
SW
NE
359
A
A'
?
0
1 km
Peridotite
Serpentinite (>80% Ant)
Continent-derived slivers
Chlorite schist
Pseudotachylyte localities
Thrust fault

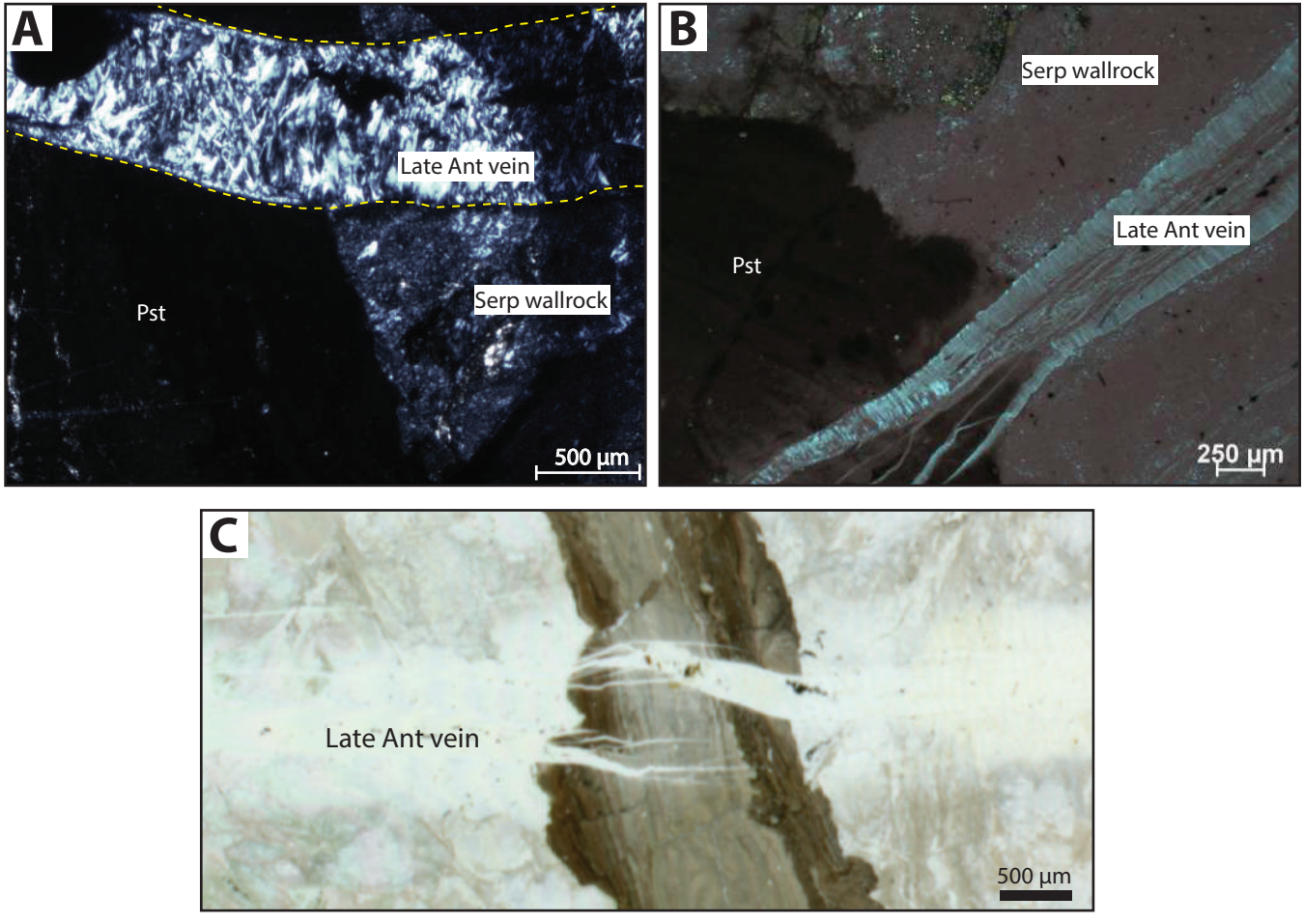
A
Late Ant vein
Pst
Serp wallrock
500 µm
B
Serp wallrock
Late Ant vein
Pst
250 µm
C
Late Ant vein
500 µm

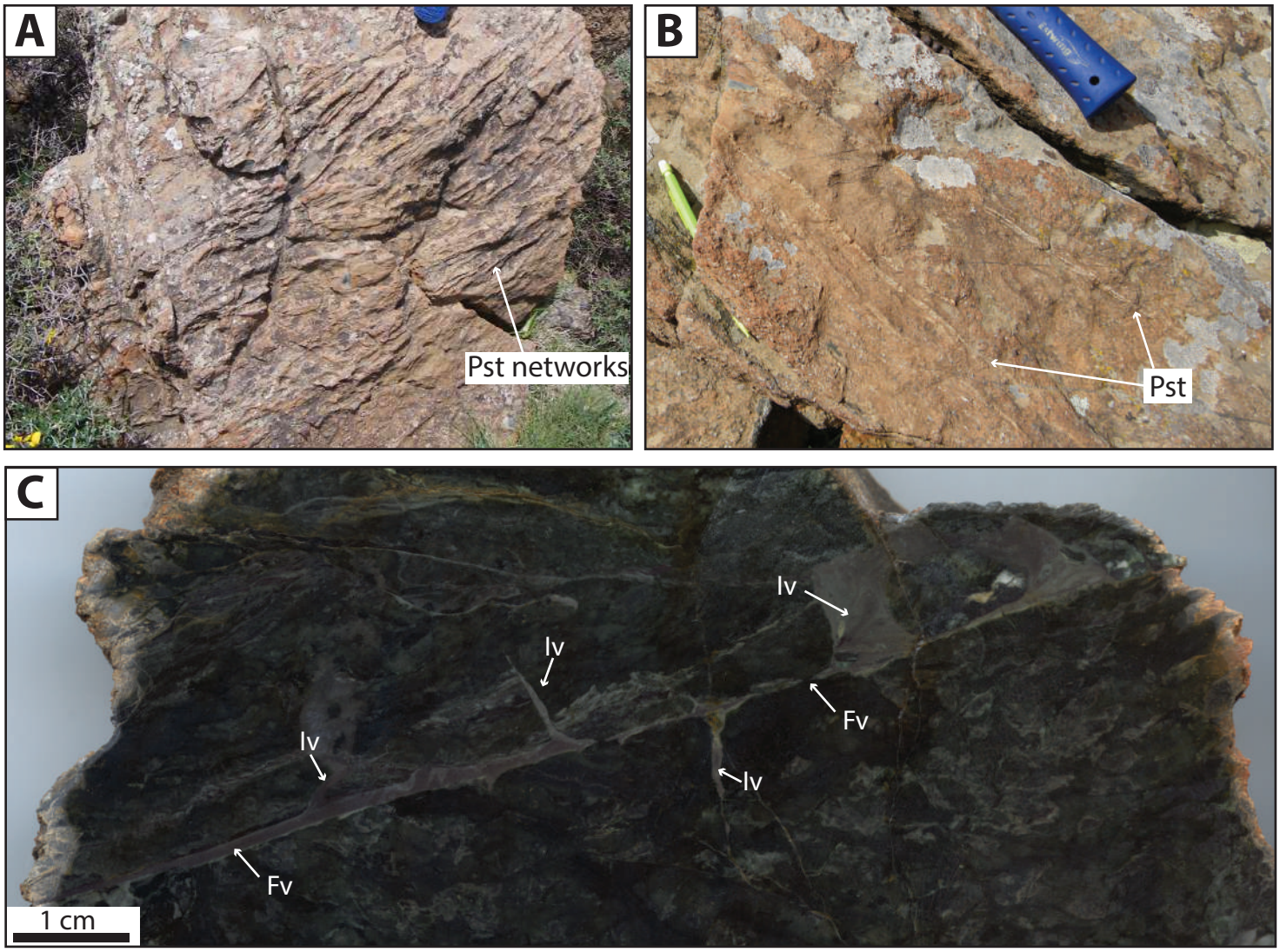
A
Pst networks
B
Pst
C
Iv
Iv
Iv
Iv
Fv
Fv
1 cm
D
Pst
Ct
Serp peridotite
Pst
1 cm

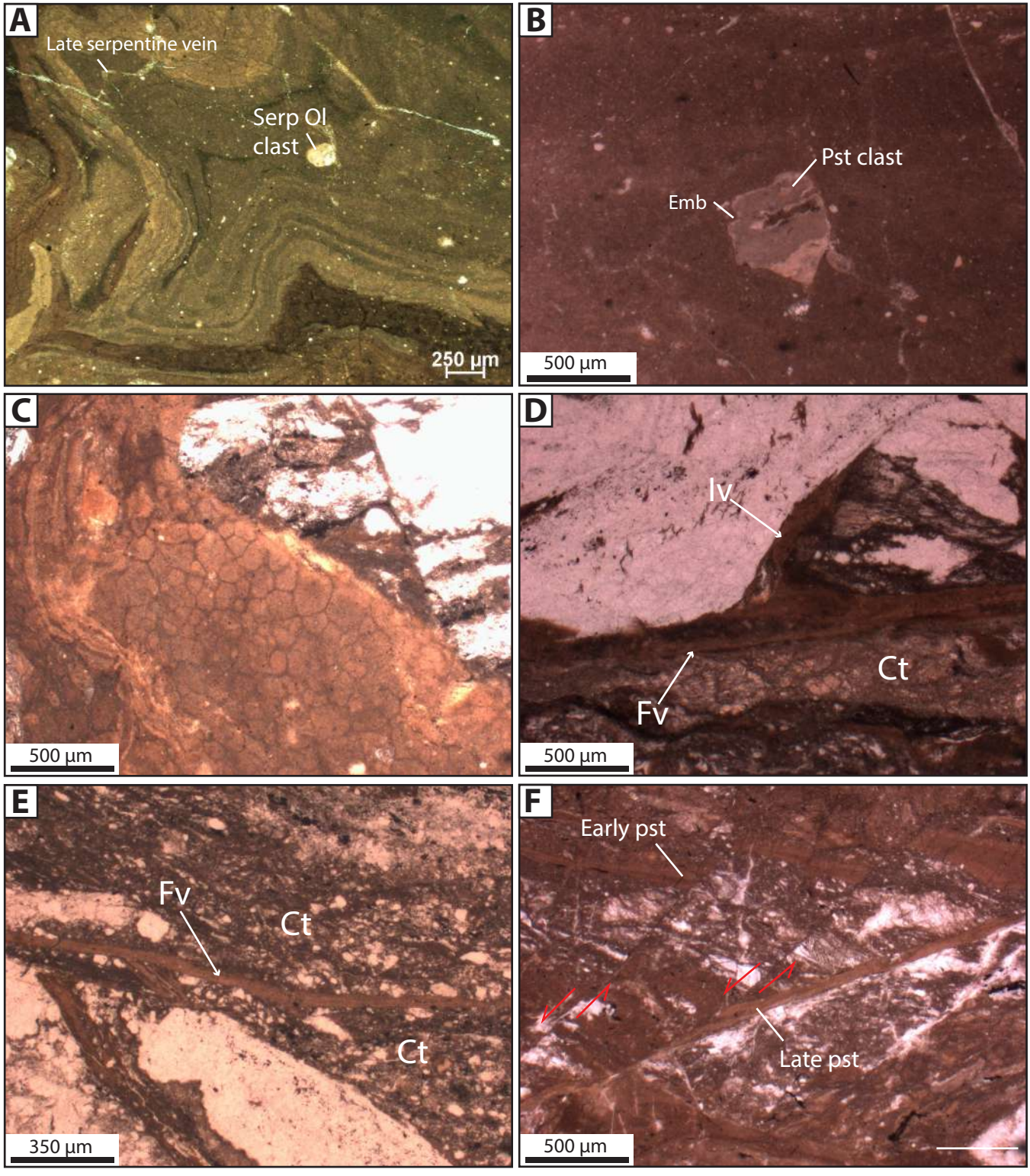
A
Late serpentine vein
Serp Ol clast
250 µm
B
Pst clast
Emb
500 µm
C
500 µm
D
Iv
Ct
Fv
500 µm
E
Fv
Ct
Ct
350 µm
F
Early pst
Late pst
500 µm

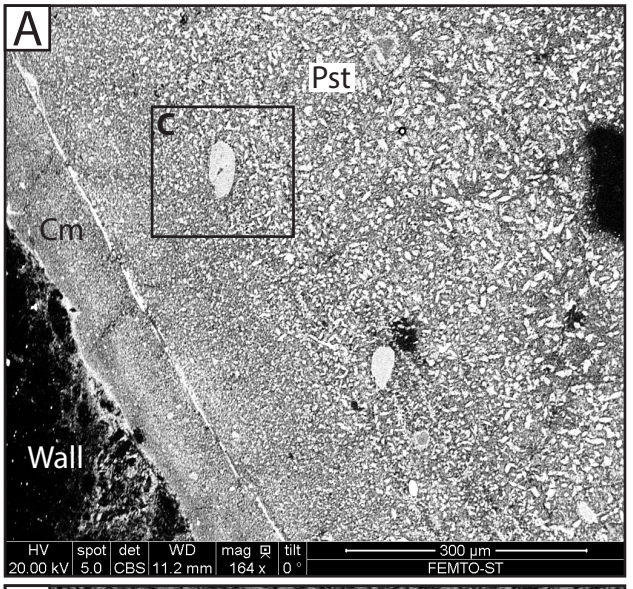
A
Pst
C
Cm
Wall
HV 20.00 kV | spot 5.0 | det CBS | WD 11.2 mm | mag 164 x | tilt 0 ° | 300 µm | FEMTO-ST

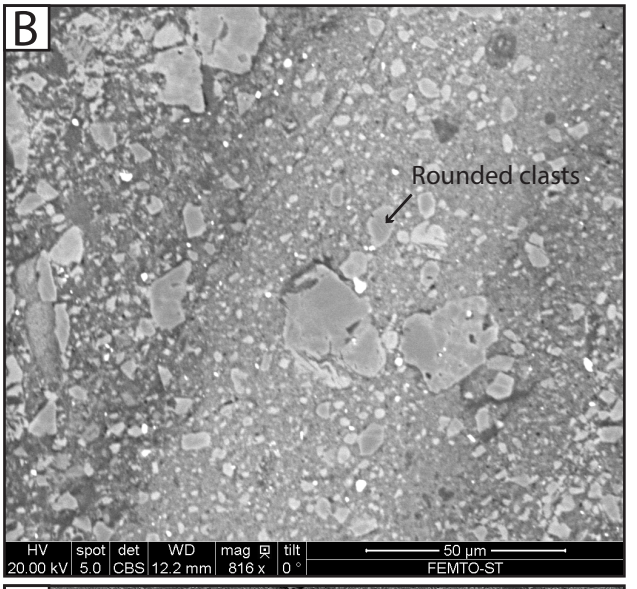
B
Rounded clasts
HV 20.00 kV | spot 5.0 | det CBS | WD 12.2 mm | mag 816 x | tilt 0 ° | 50 µm | FEMTO-ST

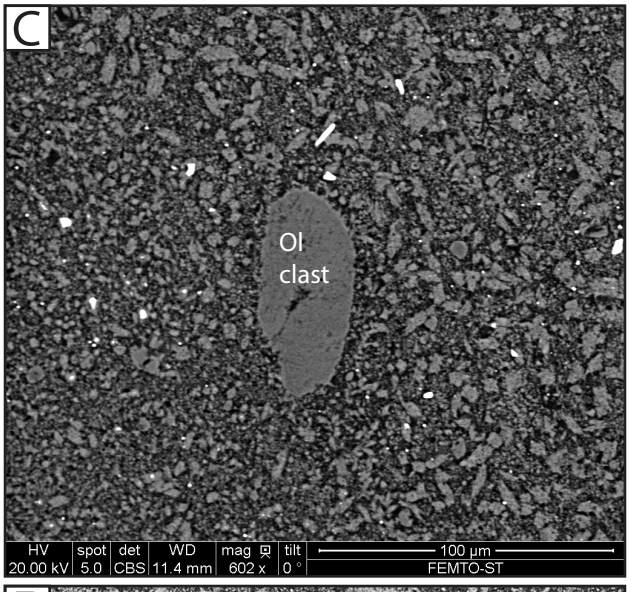
C
Ol clast
HV 20.00 kV | spot 5.0 | det CBS | WD 11.4 mm | mag 602 x | tilt 0 ° | 100 µm | FEMTO-ST

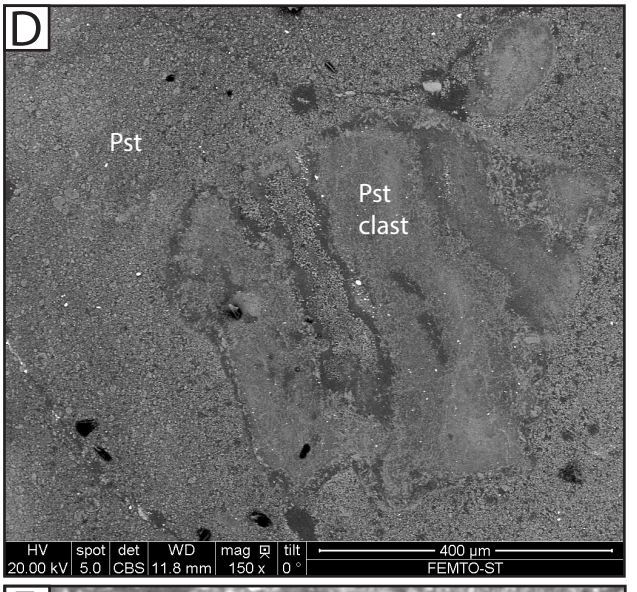
D
Pst
Pst clast
HV 20.00 kV | spot 5.0 | det CBS | WD 11.8 mm | mag 150 x | tilt 0 ° | 400 µm | FEMTO-ST

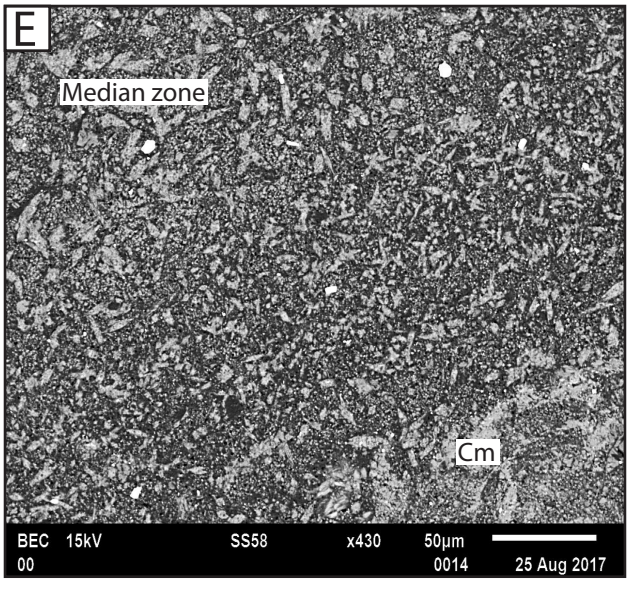
E
Median zone
Cm
BEC 15kV SS58 x430 50µm
00 0014 25 Aug 2017

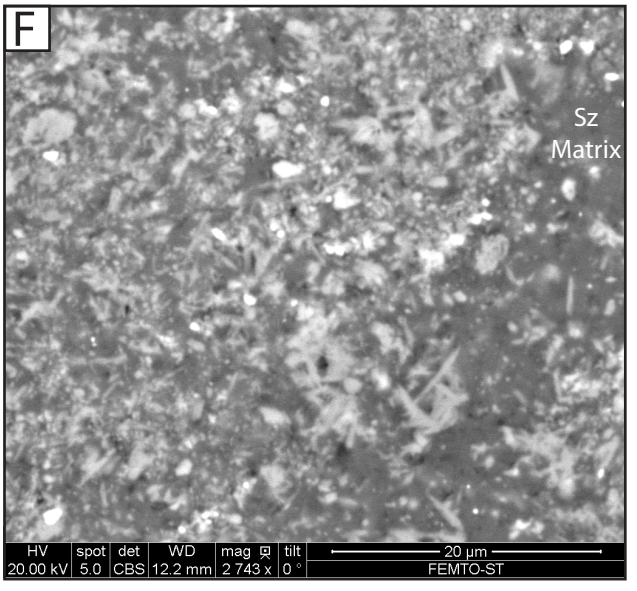
F
Sz Matrix
HV 20.00 kV | spot 5.0 | det CBS | WD 12.2 mm | mag 2 743 x | tilt 0 ° | 20 µm | FEMTO-ST

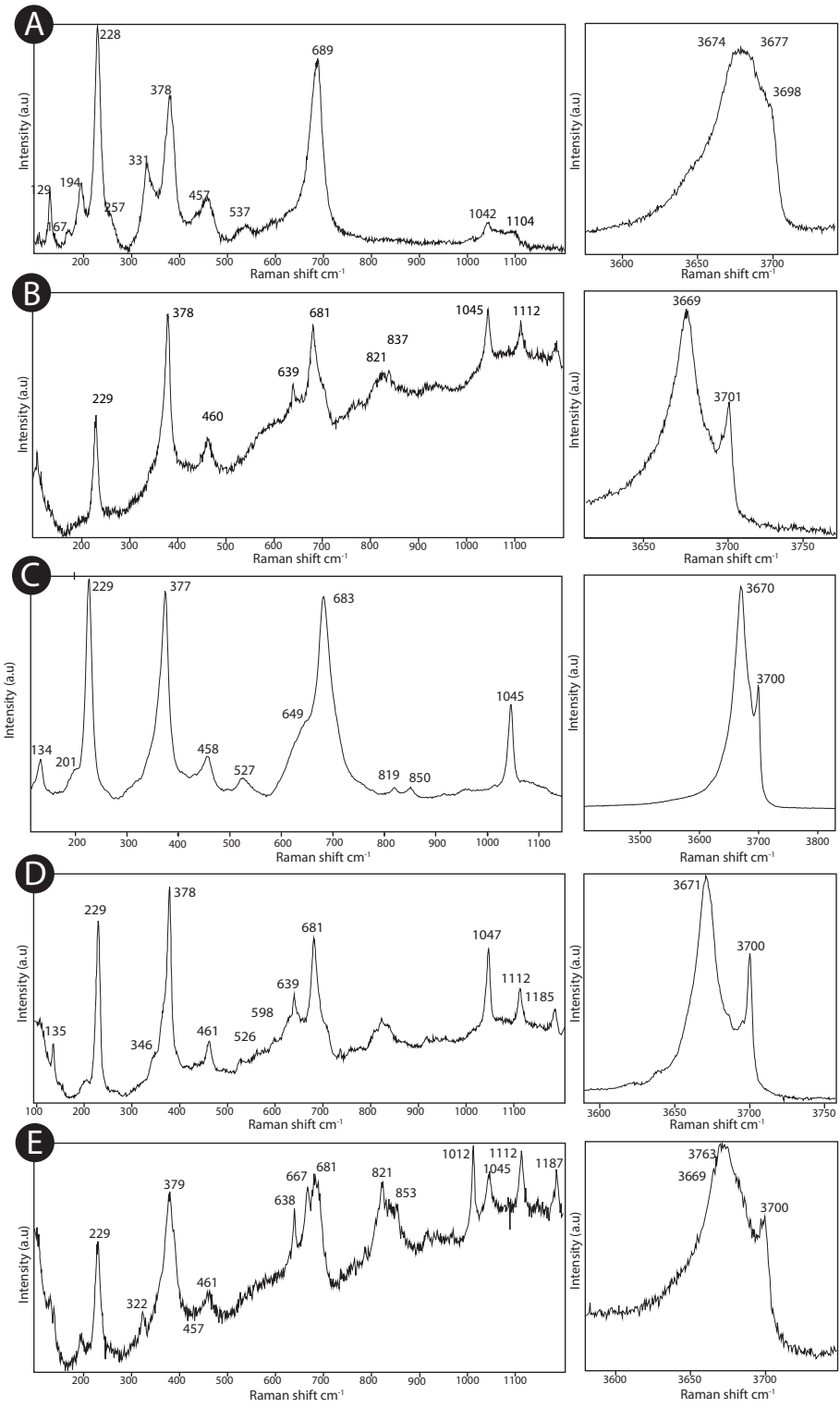
A
228
689
378
331
194
129
257
457
537
167
1042
1104
Intensity (a.u)
Raman shift cm-1
3674
3677
3698
B
378
681
1045
1112
837
821
639
229
460
3669
3701
C
229
377
683
649
1045
134
201
458
527
819
850
3670
3700
D
229
378
681
1047
639
1112
1185
598
135
346
461
526
3671
3700
E
379
667
681
821
1012
1112
1045
1187
638
853
229
322
461
457
3763
3669
3700

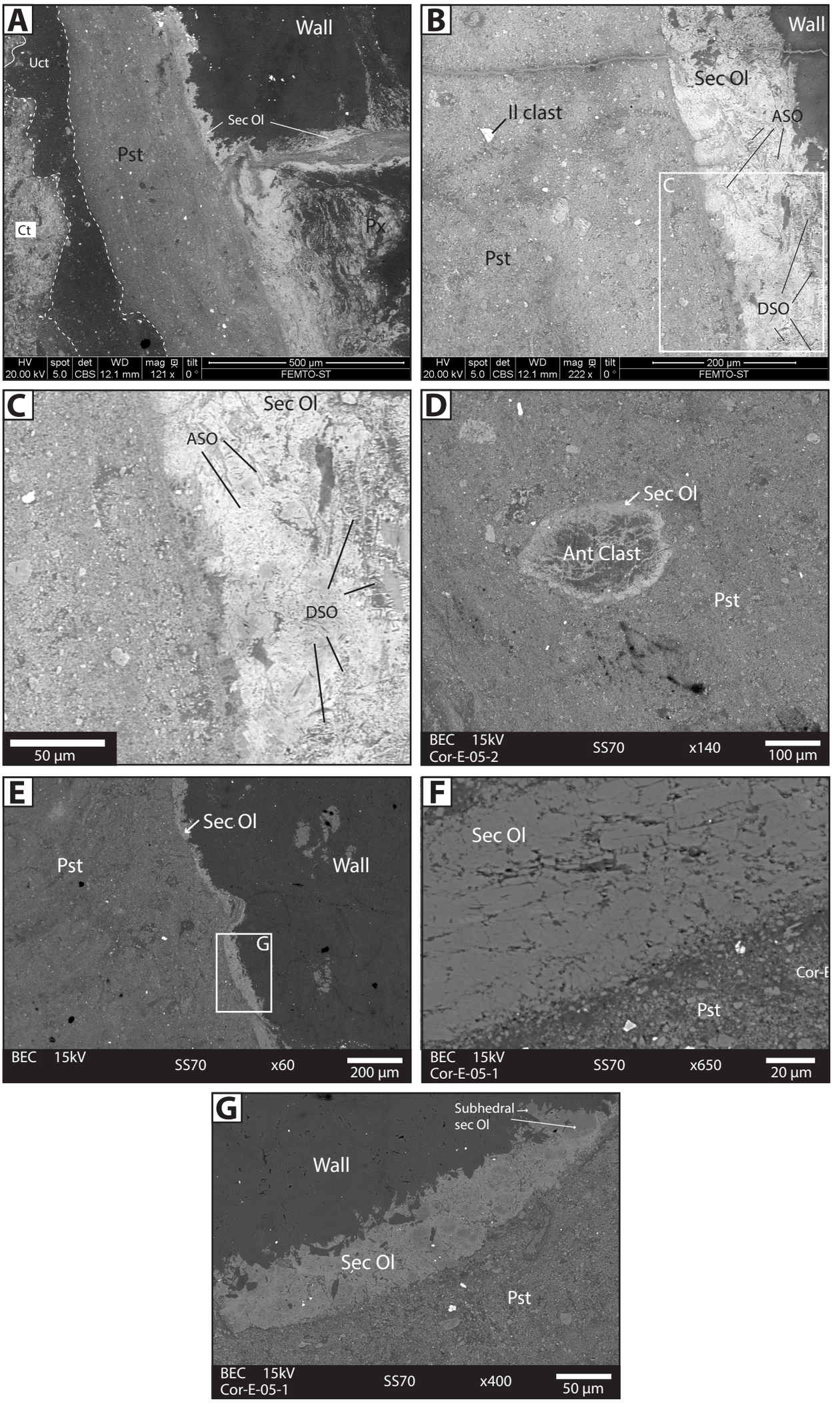
A
Wall
Uct
Sec Ol
Pst
Px
Ct
HV 20.00 kV | spot 5.0 | det CBS | WD 12.1 mm | mag 121 x | tilt 0 ° | 500 µm | FEMTO-ST
B
Wall
Sec Ol
Il clast
ASO
C
Pst
DSO
HV 20.00 kV | spot 5.0 | det CBS | WD 12.1 mm | mag 222 x | tilt 0 ° | 200 µm | FEMTO-ST
C
Sec Ol
ASO
DSO
50 µm
D
Sec Ol
Ant Clast
Pst
BEC 15kV Cor-E-05-2 SS70 x140 100 µm
E
Sec Ol
Pst
Wall
G
BEC 15kV SS70 x60 200 µm
F
Sec Ol
Cor-E
Pst
BEC 15kV Cor-E-05-1 SS70 x650 20 µm
G
Subhedral sec Ol
Wall
Sec Ol
Pst
BEC 15kV Cor-E-05-1 SS70 x400 50 µm

A

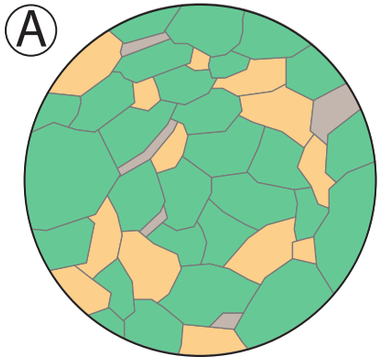

Starting rock: plagioclase lherzolite

B

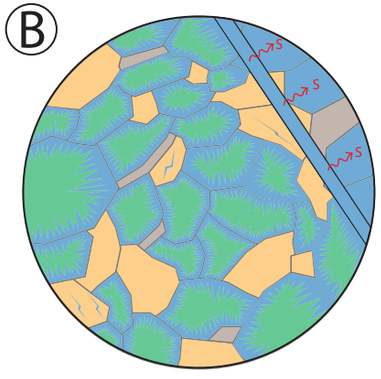

Ocean-floor serpentinization

- Progressive serpentinization (stages S1, S2, S3)
- Lizardite + chrysotile veins and diffuse serpentinization

Serpentinization propagation (along veins and grain boundaries)

C

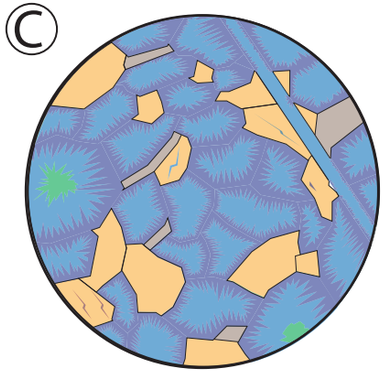

Diffuse antigoritization (S4a)

- Dehydration along grain boundaries and substitution of S1+ S2 + S3 lizardite + chrysotile by antigorite.

D

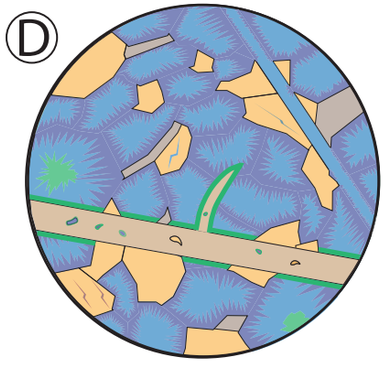

Seismic rupture and associated boundary dehydration

- Formation of pseudotachylyte
- Dehydration of serpentinite margins

E

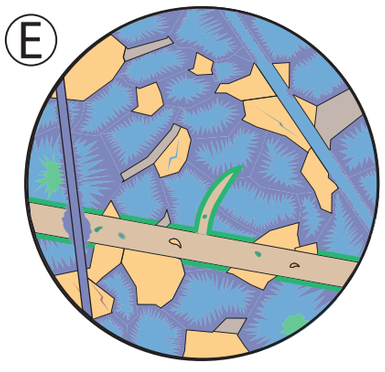

Formation of post-seismic antigorite veins (S4b)

- Release of water following host-margin dehydration
- Formation of antigorite veins
- Serpentinization of pseudotachylyte in the vicinity of antigorite vein

Mineralogy

- Olivine
- Pyroxene
- Al-bearing minerals
- S1 to S3 stages of serpentinization
- Late stage antigorite serpentinization (S4)

Pseudotachylytes

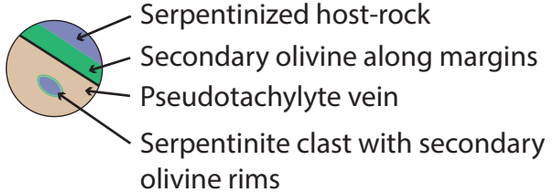

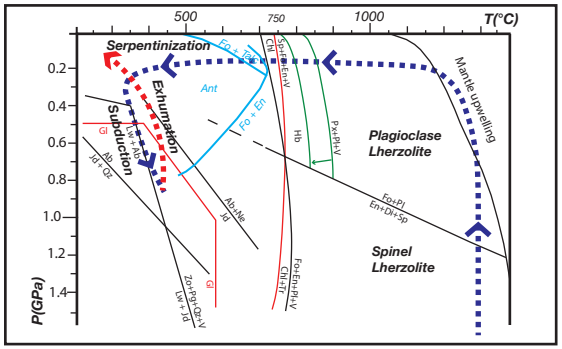
500
750
1000
T(°C)
P(GPa)
0.2
0.4
0.6
0.8
1.0
1.2
1.4
Serpentinization
Exhumation
Subduction
Mantle upwelling
Plagioclase
Lherzolite
Spinel
Lherzolite
Ant
Fo + En
Hb
Prg+Pl+V
Fo+Pl
En+Dh+Sp
Fo+En+Pl+V
Gl
Ab
Jd + Qz
Ab+Ne
Ab
Zo+Prg+Qz+V
Lw + Jd
Chl+Fo+En+V
Chl+Fo+En+V

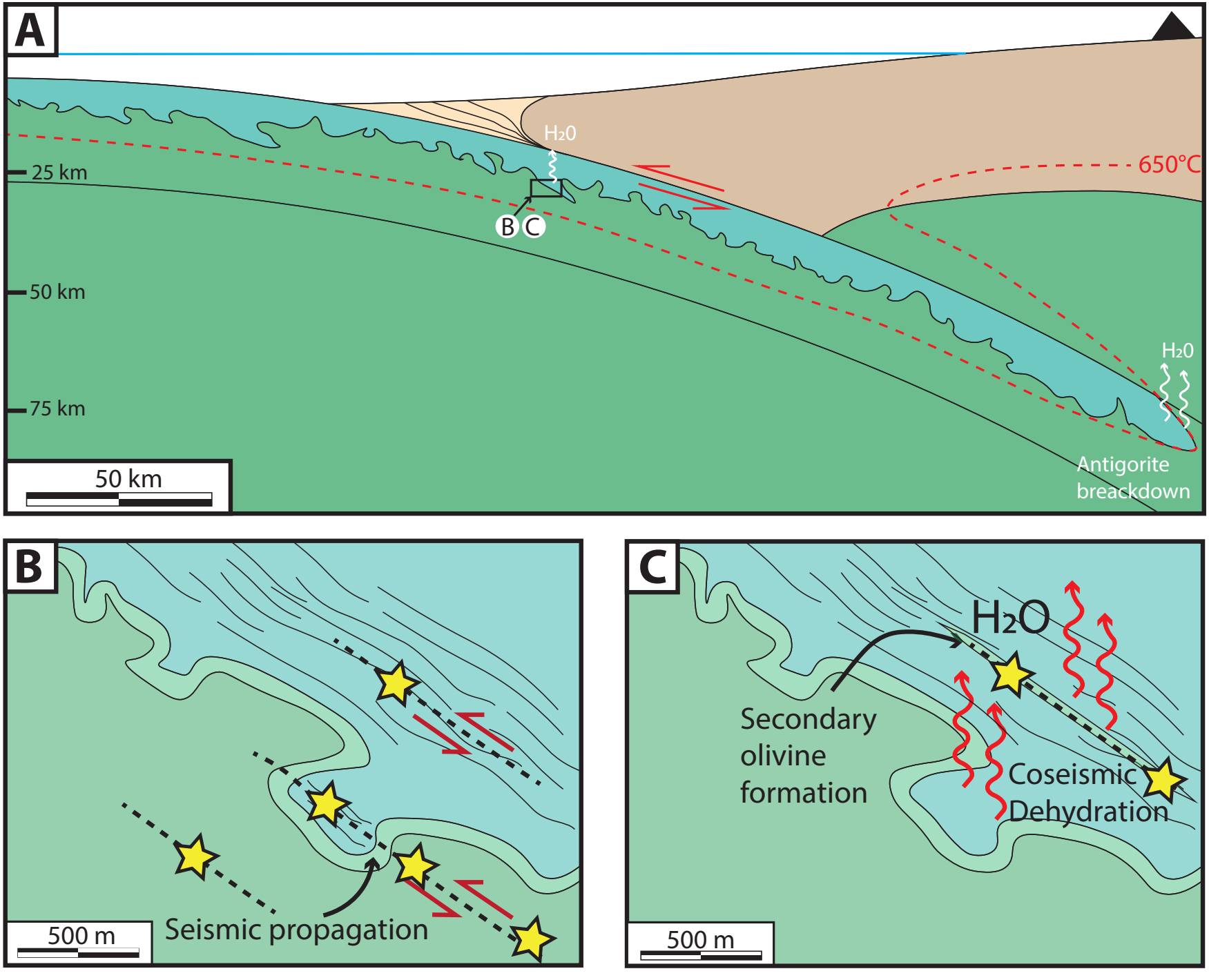
A
H20
25 km
650°C
B
C
50 km
75 km
50 km
H20
Antigorite
breackdown
B
500 m
Seismic propagation
C
H2O
Secondary
olivine
formation
Coseismic
Dehydration
500 m

Host-rock and Dehydrated border

wt.% analysis	Border Olivine	Border Olivine	Border Olivine (dark)	Border Olivine (light)	US Host rock Olivine	US Host rock Olivine	US Host rock Opx	US Host rock Cpx	SZ Host rock Serp-Ant	SZ Host rock Serp-Ant
SiO2	39.28	38.45	41.23	39.88	40.95	40.65	54.84	54.86	44.36	44.22
MgO	41.26	37.6	43.38	39.45	50.85	49.95	32.68	23.41	39.88	39.38
FeO	18.69	23.51	14.4	21.75	10.64	9.27	6.01	4.04	4.55	4.85
Al2O3	0.23	0.1	0	0.23	0	0.17	4.03	5.42	0.82	0.65
Na2O	0	0	0	0	0	0	0.03	0.39	0	0.02
CaO	0	0	0	0	0	0.09	1.31	12.33	0.03	0
K2O	0	0	0	0	0	0	0	0	0.02	0.01
MnO	0.57	1	0.8	0	0.24	0	0.11	0.02	0.05	0.06
TiO2	0	0	0	0.12	0	0	0.06	0.18	0.04	0.02
Cr2O3	0	0	0	0	0	0.04	0.61	0	0.02	0
NiO	0.12	0.17	0.11	0.22	0.38	0	0	0.03	0.17	0.07
Total	100.15	100.83	99.92	101.65	103.06	100.17	99.68	100.68	89.94	89.28
Mg #	68.82	61.53	74.05	64.46	82.37	84.35			89.66	88.91

Pseudotachylytes

wt.% analysis	Microlite Cpx	Microlite Cpx	Microlite Cpx	Matrix	Matrix	Clast Cpx	Clast Ol	Clast Serp-Ol	Clast Ilmenite
SiO2	52	49.77	51.52	40.11	39.48	52.15	40.84	40.08	2.51
MgO	17.35	26.97	17.3	32.37	34.31	13.42	51.01	40.8	2.86
FeO	7.03	3.17	6.55	8.69	12.23	10.59	10.65	8.22	39.87
Al2O3	1.37	3.5	2.46	6.52	5.72	0.84	0	2.15	0.78
Na2O	0	0.58	0.24	0.11	0	0.18	0	0	0
CaO	22.42	11.73	21.17	3.76	2.91	23.43	0	0.1	0
K2O	0.02	0	0	0	0	0	0	0	0
MnO	0	0.13	0	0.2	0.39	0.3	0.21	0.17	2.9
TiO2	0	0.16	0.26	0.31	0.23	0	0	0.08	51.33
Cr2O3	0.1	0.17	0	0.29	0.15	0	0	0.1	0
NiO	0.15	0	0.21	0.12	0.08	0	0.32	0.08	0
Total	100.44	96.18	99.71	92.48	95.5	100.91	103.05	91.77	100.25
% Fo	/	/	/	/	/		82.40	82.94	/